

Probabilistic Hierarchical Interpolation and Interpretable Configuration for Flood Prediction

Mostafa Saberian¹, Vidya Samadi^{2*}, Ioana Popescu³

1. The Glenn Department of Civil Engineering, Clemson University, Clemson, SC
2. Department of Agricultural Sciences, Clemson University, Clemson, SC.

partment of Hydroinformatics and Socio-Technical Innovation, IHE Delft Institute for Water

*Corresponding author: samadi@clemson.edu

Abstract

The last few years have witnessed the rise of neural networks (NNs) applications for hydrological time series modeling. By virtue of their capabilities, NN models can achieve unprecedented levels of performance when learn how to solve increasingly complex rainfall-runoff processes via data, making them pivotal for the development of computational hydrologic tasks such as flood predictions. The NN models should, in order to be considered practical, provide a probabilistic understanding of the model mechanisms and predictions and hints on what could perturb the model. In this paper, we developed two probabilistic NN models, i.e., Neural Hierarchical Interpolation for Time Series Forecasting (N-HiTS) and Network-Based Expansion Analysis for Interpretable Time Series Forecasting (N-BEATS) and benchmarked them with long short-term memory (LSTM) for flood prediction across two headwater streams in Georgia and North Carolina, USA. To generate a probabilistic prediction, a Multi-Quantile Loss was used to assess the 95th percentile prediction uncertainty (95PPU) of multiple flooding events. We conducted extensive flood prediction experiments demonstrating the advantages of hierarchical interpolation and interpretable architecture, where both N-HiTS and N-BEATS provided an average accuracy improvement of almost 5% (NSE) over the LSTM benchmarking model. On a variety of flooding events, both N-HiTS and N-BEATS demonstrated significant performance improvements over the LSTM benchmark and showcased their probabilistic predictions by specifying a likelihood parameter.

Keywords: Probabilistic Flood Prediction; Neural Networks; N-HiTS; N-BEATS; LSTM; Headwater Stream.

Key Points

- N-HiTS and N-BEATS predictions reflect interpretability and hierarchical representations of data to reduce neural network complexities.
- Both N-HiTS and N-BEATS models outperformed the LSTM in mathematically defining uncertainty bands.
- Predicting the magnitude of the recession curve of flood hydrographs was particularly challenging for all models.

34 **Plain Language Summary**

35 Recent progress in NN accelerated improvements in the performance of catchment modeling. Yet flood
36 modeling remains a very difficult task. Focusing on two headwater streams, we developed N-HiTS and N-
37 BEATS models and benchmarked them with LSTM to predict flooding. N-HiTS and N-BEATS
38 outperformed LSTM for flood predictions. We demonstrated how the proposed models can be augmented
39 with an uncertainty approach to predict flooding that is interpretable without considerable loss in accuracy.
40

41 **1. Introduction**

42 The last few years have been characterized by an upsurge in the neural networks (NN) applications in
43 hydrology. As opaque NN models are increasingly being employed to make important hydrological
44 predictions, the demand for creating legitimate NN models is increasing in the hydrology community.

45 However, maintaining coherence while producing accurate predictions can be a challenging problem
46 (Olivares et al., 2024). There is a general agreement on the importance of providing probabilistic NN
47 prediction (Samadi et al., 2020), especially in the case of flood prediction (Martinaitis et al., 2023).

48 Flood occurrences have witnessed an alarming surge in frequency and severity globally. Jonkman (2005)
49 studied a natural disaster database (EM-DAT, 2023) and reported that over 27 years, more than 175000
50 people died, and close to 2.2 billion were affected directly by floods worldwide. These numbers are likely
51 an underestimation due to unreported events (Nevo et al., 2022). In addition, the United Nations Office for
52 Disaster Risk Reduction reported that flooding has been the most frequent, widespread weather-related
53 natural disaster since 1995, claiming over 600,000 lives, affecting around 4 billion people globally, and
54 causing annual economic damage of more than 100 billion USD (UNISDR, 2015). This escalating trend
55 has necessitated the need for better flood prediction and management strategies. Scholars have successfully
56 implemented different flood models such as deterministic (e.g., Roelvink et al., 2009, Thompson and
57 Frazier, 2014; Barnard et al., 2014; Erikson et al., 2018) and physically based flood models (e.g., Basso et
58 al., 2016; Chen et al., 2016; Pourreza-Bilondi et al., 2017; Saksena et al., 2019; Refsgaard et al., 2021) in
59 various environmental systems over the past several decades. These studies have heightened the need for
60 precise flood prediction, they have also unveiled limitations inherent in existing deterministic and physics-
61 based models. While evidence suggests that both deterministic and physics-based approaches are
62 meaningful and useful (Sukovich et al., 2014; Zafarmomen et al., 2024), their forecasts rest heavily on
63 imprecise and subjective expert opinion; there is a challenge for setting robust evidence-based thresholds
64 to issue flood warnings and alerts (Palmer, 2012). Moreover, many of these traditional flood models
65 particularly physically explicit models rely heavily on a particular choice of numerical approximation and
66 describe multiple process parameterizations only within a fixed spatial architecture (e.g., Clark et al., 2015).

67 Recent NN models have shown promising results across a large variety of flood modeling applications (e.g.,

68 Nevo et al., 2022; Pally and Samadi, 2022; Dasgupta et al., 2023; Zhang et al., 2023) and encourage the
69 use of such methodologies as core drivers for neural flood prediction (Windheuser et al., 2023).
70 Earlier adaptations of these intelligent techniques showed promising for flood prediction (e.g., Hsu et al.,
71 1995; Tiwari and Chatterjee, 2010). However, recent efforts have taken NN application to the next level,
72 providing uncertainty assessment (Sadeghi Tabas and Samadi, 2022) and improvements over various
73 spatio-temporal scales, regions, and processes (e.g., Kratzert et al., 2018; Park and Lee, 2023; Zhang et al.,
74 2023). Nevo et al., (2022) were the first scholars who employed long short-term memory (LSTM) for flood
75 stage prediction and inundation mapping, achieving notable success during the 2021 monsoon season. Soon
76 after, Russo et al. (2023) evaluated various NN models for predicting flood depth in urban systems,
77 highlighting the potential of data-driven models for urban flood prediction. Similarly, Defontaine et al.
78 (2023) emphasized the role of NN algorithms in enhancing the reliability of flood predictions, particularly
79 in the context of limited data availability. Windheuser et al., (2023) studied flood gauge height forecasting
80 using images and time series data for two gauging stations in Georgia, USA. They used multiple NN models
81 such as Convolutional Neural Network (ConvNet/CNN) and LSTM to forecast floods in near real-time (up
82 to 72 hours). In a sequence, Wee et al., (2023) used Impact-Based Forecasting (IBF) to propose a Flood
83 Impact-Based Forecasting system (FIBF) using flexible fuzzy inference techniques, aiding decision-makers
84 in a timely response. Zou et al. (2023) proposed a Residual LSTM (ResLSTM) model to enhance and
85 address flood prediction gradient issues. They integrated Deep Autoregressive Recurrent (DeepAR) with
86 four recurrent neural networks (RNNs), including ResLSTM, LSTM, Gated Recurrent Unit (GRU), and
87 Time Feedforward Connections Single Gate Recurrent Unit (TFC-SGRU). They showed that ResLSTM
88 achieved superior accuracy. While these studies reported the superiority of NN models for flood modeling,
89 they highlighted a number of challenges, notably (i) the limited capability of proposed NN models to
90 capture the spatial variability and magnitudes of extreme data over time, (ii) the lack of a sophisticated
91 mechanism to capture different flood magnitudes and synthesize the prediction, and (iii) inability of the NN
92 models to process data in parallel and capture the relationships between all elements in a sequential manner.
93 Recent advances in neural time series forecasting showed promising results that can be used to address the
94 above challenges for flood prediction. Recent techniques include the adoption of the attention mechanism
95 and Transformer-inspired approaches (Fan et al. 2019; Alaa and van der Schaar 2019; Lim et al. 2021)
96 along with attention-free architectures composed of deep stacks of fully connected layers (Oreshkin et al.
97 2020). All of these approaches are relatively easy to scale up in terms of flood magnitudes (small to major
98 flood predictions), compared to LSTM and have proven to be capable of capturing spatiotemporal
99 dependencies (Challu et al., 2022). In addition, these architectures can capture input-output relationships
100 implicitly while they tend to be more computationally efficient. Many state-of-the-art NN approaches for
101 flood forecasting have been established based on LSTM. There are cell states in the LSTM networks that

102 can be interpreted as storage capacity often used in flood generation schemes. In LSTM, the updating of
103 internal cell states (or storages) is regulated through a number of gates: the first gate regulates the storage
104 depletion, the second one regulates storage fluctuations, and the third gate regulates the storages outflow
105 (Tabas and Samadi, 2022). The elaborate gated design of the LSTM partly solves the long-term dependency
106 problem in flood time series prediction (Fang et al., 2020), although, the structure of LSTMs is designed in
107 a sequential manner that cannot directly connect two nonadjacent portions (positions) of a time series.

108 In this paper, we developed attention-free architecture, i.e. Neural Hierarchical Interpolation for Time
109 Series Forecasting (N-HiTS; Challu et al., 2022) and Network-Based Expansion Analysis for Interpretable
110 Time Series Forecasting (N-BEATS; Oreshkin et al., 2020) and benchmarked these models with LSTM for
111 flood prediction. We developed fully connected N-BEATS and N-HiTS architectures using multi-rate data
112 sampling, synthesizing the flood prediction outputs via multi-scale interpolation.

113 We implemented all algorithms for flood prediction on two headwater streams i.e., the Lower Dog River,
114 Georgia, and the Upper Dutchmans Creek, North Carolina, USA to ensure that the results are reliable and
115 comparable. The results of N-BEATS and N-HiTS techniques were compared with the benchmarking
116 LSTM to understand how these techniques can improve the representations of rainfall and runoff
117 dispensing over a recurrence process. Notably, this study represents a pioneering effort, as to the best of
118 our knowledge, this is the first instance in which the application of N-BEATS and N-HiTS algorithms in
119 the field of flood prediction has been explored. The scope of this research will focus on:

120

121 **(i) Flood prediction in a hierarchical fashion with interpretable outputs:** We built N-BEATS and N-
122 HiTS for flood prediction with a very deep stack of fully connected layers to implicitly capture input-output
123 relationships with hierarchical interpolation capabilities. The predictions also involve programming the
124 algorithms with decreasing complexity and aligning their time scale with the final output through multi-
125 scale hierarchical interpolation and interpretable architecture. Predictions were aggregated in a hierarchical
126 fashion that enabled the building of a very deep neural network with interpretable configurations.

127 **(ii) Uncertainty quantification of the models by employing probabilistic approaches:** a Multi-
128 Quantile Loss (MQL) was used to assess the 95th percentile prediction uncertainty (95PPU) of multiple
129 flooding events. MQL was integrated as the loss function to account for probabilistic prediction. MQL
130 trains the model to produce probabilistic forecasts by predicting multiple quantiles of the distribution of
131 future values.

132 **(iii) Exploring headwater stream response to flooding:** Understanding the dynamic response of
133 headwater streams to flooding is essential for managing downstream flood risks. Headwater streams
134 constitute the uppermost sections of stream networks, usually comprising 60% to 80% of a catchment area.
135 Given this substantial coverage and the tendency for precipitation to increase with elevation, headwater

136 streams are responsible for generating and controlling the majority of runoff in downstream portions
137 (MacDonald and Coe, 2007).

138 The remainder of this paper is structured as follows. Section 2 presents the case study and data, NN models,
139 performance metrics, and sensitivity and uncertainty approaches. Section 3 focuses on the results of flood
140 predictions including sensitivity and uncertainty assessment and computation efficiency. Finally, Section 4
141 concludes the paper.

142

143 **2. Methodology**

144 **2.1. Case Study and Data**

145 This research used two headwater gauging stations located at the Lower Dog River watershed, Georgia
146 (GA; USGS02337410, Dog River gauging station), and the Upper Dutchmans Creek watershed, North
147 Carolina (NC; USGS0214269560, Killian Creek gauging station). As depicted in Figures 1 and 2, the Lower
148 Dog River and the Upper Dutchmans Creek watersheds are located in the west and north parts of two
149 metropolitan cities, Atlanta and Charlotte. As shown in Figure 1, the Lower Dog River stream gauge is
150 established southeast of Villa Rica in Carroll County, where the USGS has regularly monitored discharge
151 data since 2007 in 15-minute increments. The Lower Dog River is a stream with a length of 15.7 miles
152 (25.3 km; obtained from the U.S. Geological Survey [USGS] National Hydrography Dataset high-
153 resolution flowline data), an average elevation of 851.94 meters, and the watershed area above this gauging
154 station is 66.5 square miles (172 km²; obtained from the Georgia Department of Natural Resources). This
155 watershed is covered by 15.2% residential area, 14.6% agricultural land, and ~70% forest (Munn et al.,
156 2020). Killian Creek gauging station at the Upper Dutchmans Creek watershed is established
157 in Montgomery County, NC, where the USGS has regularly monitored discharge data since 1995 in 15-
158 minute increments. The Upper Dutchmans Creek is a stream with a length of 4.9 miles (7.9 km), an average
159 elevation of 642.2 meters (see Table 1), and the watershed area above this gauging station is 4 square miles
160 (10.3 km²) with less than 3% residential area and about 93% forested land use (the United States
161 Environmental Protection Agency).

162 The Lower Dog River has experienced significant flooding in the last decades. For example, in September
163 2009, the creek, along with most of northern GA, experienced heavy rainfall (5 inches, equal to 94 mm).
164 The Lower Dog River, overwhelmed by large amounts of overland flow from saturated ground in the
165 watershed, experienced massive flooding in September 2009 (Gotvald, 2010). The river crested at 33.8 feet
166 (10.3 m) with a peak discharge of 59,900 cfs (1,700 m³/s), nearly six times the 100-year flood level
167 (McCallum and Gotvald, 2010). In addition, Dutchmans Creek has experienced significant flooding in
168 February 2020. According to local news (WCCB Charlotte, 2020), the flood in Gaston County caused

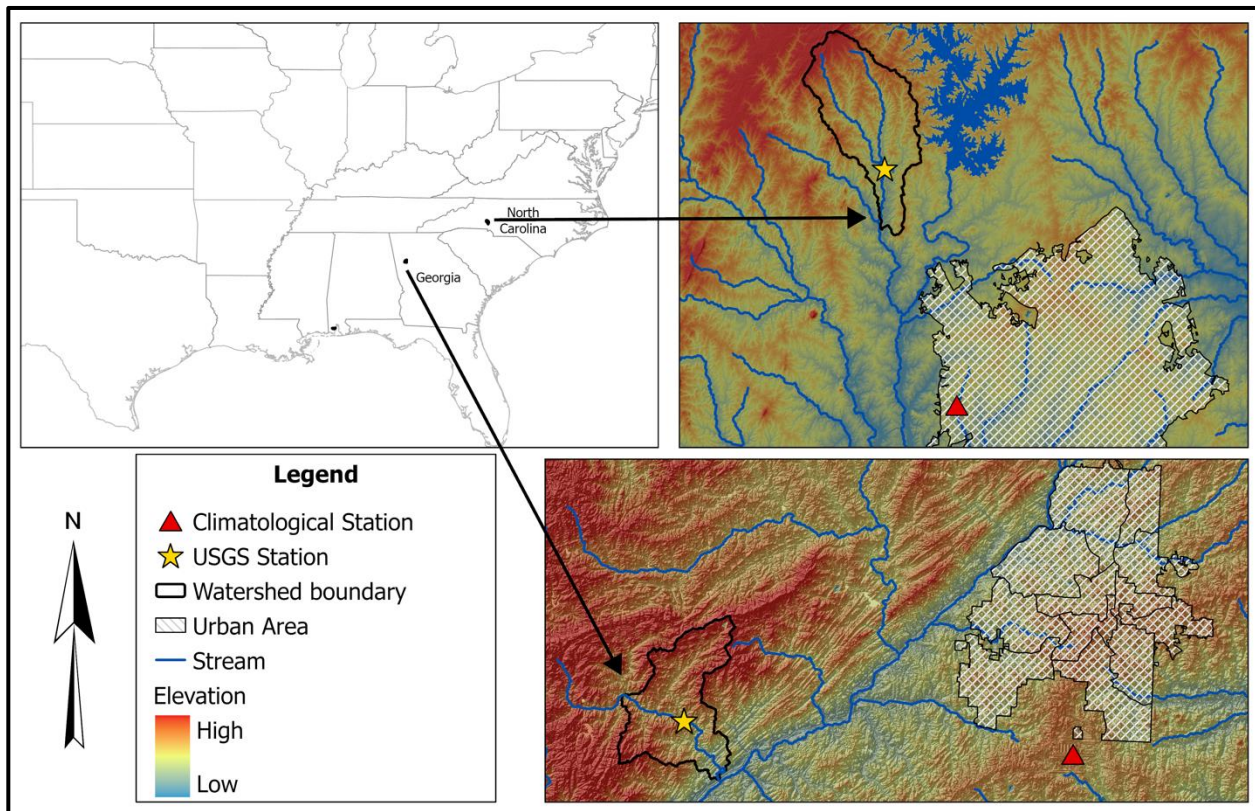
169 significant infrastructure damage and community disruption. Key impacts included the threatened collapse
170 of the Dutchman's Creek bridge in Mt. Holly and the closure of Highway 7 in McAdenville, GA.

171

172 Table 1. The Lower Dog River and Upper Dutchmans Creek's physical characteristics.

Watershed	USGS Station ID Number	Average Elevation (m)	Stream Length (km)	Watershed area (km ²)
Lower Dog River watershed, GA	USGS02337410	851.9	25.3	172
Upper Dutchmans Creek watershed, NC	USGS0214269560	642.2	7.9	10.3

173



174

175 Figure 1. The Lower Dog River and The Upper Dutchmans Creek watersheds are located in GA and NC.
176 The proximity of the watersheds to Atlanta and Charlotte (urban area) are also displayed on the map.

177

178 To provide the meteorological forcing data, i.e., precipitation, temperature, and humidity, were extracted
179 from the National Oceanic and Atmospheric Administration's (NOAA) Local Climatological Data
180 (LCD). We used the NOAA precipitation, temperature, and humidity data of Atlanta Hartsfield Jackson
181 International Airport and Charlotte Douglas Airport stations as an input variable for neural network

182 algorithms. The data has been monitored since January 1, 1948, and July 22, 1941, with an hourly interval
183 which was used as an input variable for constructing neural networks.

184 To fill in the missing values in the data, we used the spline interpolation method. We applied this method
185 to fill the gaps in time series data, although the missing values were insignificant (less than 1%). In addition,
186 we employed the Minimum Inter-Event Time (MIT) approach to precisely identify and separate individual
187 storm events. The MIT-based event delineation is pivotal for accurately defining storm events. This method
188 allowed us to isolate discrete rainfall episodes, aiding a comprehensive analysis of storm events. Moreover,
189 it provided a basis for event-specific examination of flood responses, such as initial condition and cessation
190 (loss), runoff generation, and runoff dynamics.

191 The hourly rainfall dataset consists of distinct rainfall occurrences, some consecutive and others clustered
192 with brief intervals of zero rainfall. As these zero intervals extend, we aim to categorize them into distinct
193 events. It's worth noting that even within a single storm event, we often encounter short periods of no
194 rainfall, known as intra-storm zero values. In the MIT method, we defined a storm event as a discrete rainfall
195 episode surrounded by dry periods both preceding and following it, determined by an MIT (Asquith et al.,
196 2005; Safaei-Moghadam et al., 2023). There are many means to determine an MIT value. One practical
197 approximation is using serial autocorrelation between rainfall occurrences. MIT approach uses
198 autocorrelation that measures the statistical dependency of rainfall data at one point in time with data at
199 earlier, or lagged times within the time series. The lag time represents the gap between data points being
200 correlated. When the lag time is zero, the autocorrelation coefficient is unity, indicating a one-to-one
201 correlation. As the lag time increases, the statistical correlation diminishes, converging to a minimum value.
202 This signifies the fact that rainfall events become progressively less statistically dependent or, in other
203 words, temporally unrelated. To pinpoint the optimal MIT, we analyzed the autocorrelation coefficients for
204 various lag times, observing the point at which the coefficient approaches zero. This lag time signifies the
205 minimum interval of no rainfall, effectively delineating distinct rainfall events.

206 **2.2. NN Algorithms**

207 **2.2.1. LSTM**

208 LSTM is an RNN architecture widely used as a benchmark model for flood neural time series
209 modeling. LSTM networks are capable of selectively learning order dependence in sequence prediction
210 problems (Sadeghi Tabas and Samadi, 2022). These networks are powerful because they can capture the
211 temporal features, especially the long-term dependencies (Hochreiter et al., 2001), and are independent of
212 the length of the input data sequences meaning that each sample is independent from another one.

213 The memory cell state within LSTM plays a crucial role in capturing extended patterns in data, making it
214 well-suited for dynamic time series modeling such as flood prediction. An LSTM cell uses the following
215 functions to compute flood prediction.

$$i_t = \sigma(A_i x_t + B_i h_{t-1} + c_i) \quad (\text{Equation 1})$$

$$f_t = \sigma(A_f x_t + B_f h_{t-1} + c_f) \quad (\text{Equation 2})$$

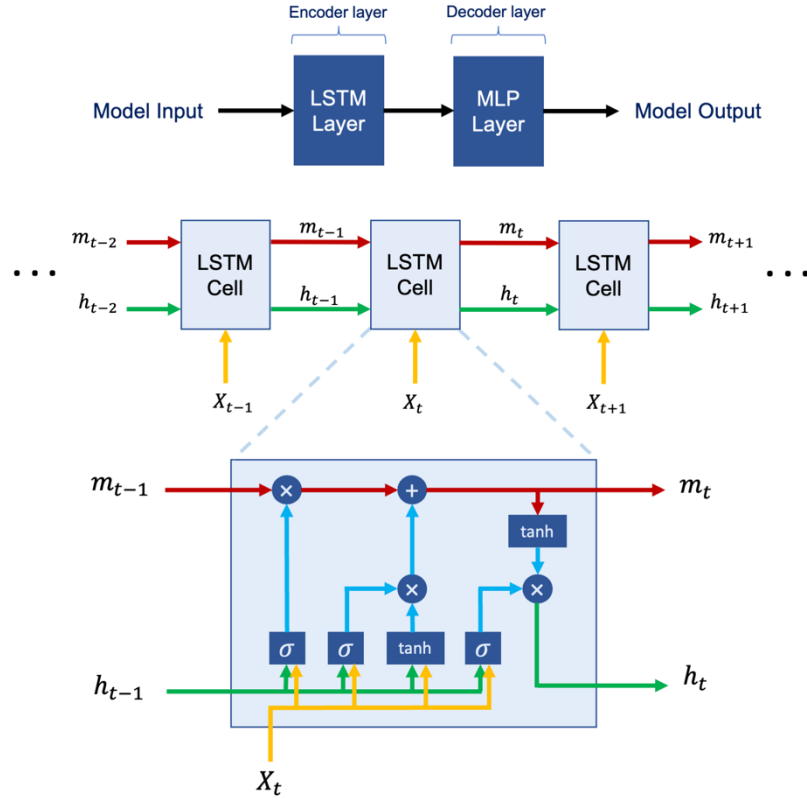
$$o_t = \sigma(A_o x_t + B_o h_{t-1} + c_o) \quad (\text{Equation 3})$$

$$m_t = f_t \odot m_{t-1} + i_t \odot \tanh(A_g x_t + B_g h_{t-1} + c_g) \quad (\text{Equation 4})$$

$$h_t = o_t \odot \tanh(m_t) \quad (\text{Equation 5})$$

216 Where x_t and h_t represent the input and the hidden state at time step t , respectively. \odot denotes element-
217 wise multiplication, \tanh stands for the hyperbolic tangent activation function, and σ represents the
218 sigmoid activation function. A , B , and c are trainable weights and biases that undergo optimization during
219 the training process. m_t and h_t are cell states at time step t that are employed in the input processing for
220 the next time step. m_t represents the memory state responsible for preserving long-term information, while
221 h_t represents the memory state preserving short-term information. The LSTM cell consists of a forget gate
222 f_t , an input gate i_t and an output gate o_t and has a cell state m_t . At every time step t , the cell gets the data
223 point x_t with the output of the previous cell h_{t-1} (Windheuser et al., 2023). The forget gate then defines if
224 the information is removed from the cell state, while the input gate evaluates if the information should be
225 added to the cell state and the output gate specifies which information from the cell state can be used for
226 the next cells.

227 We used two LSTM layers with 128 cells in the first two hidden layers as encoder layers, which were then
228 connected to two multilayer perceptron (MLP) layers with 128 neurons as decoder layers. The LSTM
229 simulation was performed with these input layers along with the *Adam* optimizer (Kingma and Ba,
230 2014), \tanh activation function, and a single lagged dependent-variable value to train with a learning rate
231 of 0.001. The architecture of the proposed LSTM model is illustrated in Figure 2.



232
233
234
235

236 **2.2.2. N-BEATS**

237 N-BEATS is a deep learning architecture based on backward and forward residual links and the very deep
238 stack of fully connected layers specifically designed for sequential data forecasting tasks (Oreshkin et al.,
239 2020). This architecture has a number of desirable properties including interpretability. The N-BEATS
240 architecture distinguishes itself from existing architectures in several ways. First, the algorithm approaches
241 forecasting as a non-linear multivariate regression problem instead of a sequence-to-sequence
242 challenge. Indeed, the core component of this architecture (as depicted in Figure 3) is a fully connected
243 non-linear regressor, which takes the historical data from a time series as input and generates multiple data
244 points for the forecasting horizon. Second, the majority of existing time series architectures are quite limited
245 in depth, typically consisting of one to five LSTM layers. N-BEATS employs the residual principle to stack
246 a substantial number of layers together, as illustrated in Figure 3. In this configuration, the basic block not
247 only predicts the next output but also assesses its contribution to decomposing the input, a concept that is
248 referred to as "backcast" (see Oreshkin et al. 2020).

249 The basic building block in the architecture features a fork-like structure, as illustrated in Figure 3 (bottom).
 250 The l -th block (for the sake of brevity, the block index l is omitted from Figure 3) takes its respective input,
 251 x_l , and produces two output vectors: \hat{x}_l and \hat{y}_l . In the initial block of the model, x_l corresponds to the
 252 overall model input, which is a historical lookback window of a specific length, culminating with the most
 253 recent observed data point. For the subsequent blocks, x_l is derived from the residual outputs of the
 254 preceding blocks. Each block generates two distinct outputs: 1. \hat{y}_l : This represents the forward forecast of
 255 the block, spanning a duration of H time units. 2. \hat{x}_l : This signifies the block's optimal estimation of x_l ,
 256 which is referred to “backcast.” This estimation is made within the constraints of the functional space
 257 available to the block for approximating signals (Oreshkin et al., 2020).

258 Internally, the fundamental building block is composed of two elements. The initial element involves a
 259 fully connected network, which generates forward expansion coefficient predictors, θ_l^f , and a backward
 260 expansion coefficient predictor, θ_l^b . The second element encompasses both backward basis layers, g_l^b , and
 261 forward basis layers, g_l^f . These layers take the corresponding forward θ_l^f and backward θ_l^b expansion
 262 coefficients as input, conduct internal transformations using a set of basis functions, and ultimately yield
 263 the backcast, \hat{x}_l , and the forecast outputs, \hat{y}_l , as previously described by Oreshkin et al. (2020). The
 264 following equations describe the first element:

$$h_{l,1} = FC_{l,1}(x_l), \quad h_{l,2} = FC_{l,2}(h_{l,1}), \quad h_{l,3} = FC_{l,3}(h_{l,2}), \quad h_{l,4} = FC_{l,4}(h_{l,3}). \quad (\text{Equation 6})$$

$$\theta_l^b = \text{LINEAR}_l^b(h_{l,4}), \quad \theta_l^f = \text{LINEAR}_l^f(h_{l,4}) \quad (\text{Equation 7})$$

265 The LINEAR layer, in essence, functions as a straightforward linear projection, meaning $\theta_l^f = W_l^f h_{l,4}$. As
 266 for the fully connected (FC) layer, it takes on the role of a conventional FC layer, incorporating RELU non-
 267 linearity as an activation function.

268 The second element performs the mapping of expansion coefficients θ_l^f and θ_l^b to produce outputs using
 269 basis layers, resulting in $\hat{y}_l = g_l^f(\theta_l^f)$ and $\hat{x}_l = g_l^b(\theta_l^b)$. This process is defined by the following equation:

$$\hat{y}_l = \sum_{i=1}^{\dim(\theta_l^f)} \theta_{l,i}^f v_i^f, \quad \hat{x}_l = \sum_{i=1}^{\dim(\theta_l^b)} \theta_{l,i}^b v_i^b \quad (\text{Equation 8})$$

270 Within this context, v_i^f and v_i^b represent the basis vectors for forecasting and backcasting, respectively,
 271 while $\theta_{l,i}^f$ corresponds to the i -th element of θ_l^f .

272 The N-BEATS uses a novel hierarchical doubly residual architecture which is illustrated in Figure 3 (top
 273 and middle). This framework incorporates two residual branches, one traversing the backcast predictions
 274 of each layer, while the other traverses the forecast branch of each layer. The following equation describes
 275 this process:

$$x_l = x_{l-1} - \hat{x}_{l-1} \quad , \quad \hat{y} = \sum_l \hat{y}_l \quad (\text{Equation 9})$$

276 As mentioned earlier, in the specific scenario of the initial block, its input corresponds to the model-level
 277 input x . In contrast, for all subsequent blocks, the backcast residual branch x_l can be conceptualized as
 278 conducting a sequential analysis of the input signal. The preceding block eliminates the portion of the signal
 279 \hat{x}_{l-1} that it can effectively approximate, thereby simplifying the prediction task for downstream blocks.
 280 Significantly, each block produces a partial forecast \hat{y}_l , which is initially aggregated at the stack level and
 281 subsequently at the overall network level, establishing a hierarchical decomposition. The ultimate forecast
 282 \hat{y} is the summation of all partial forecasts (Oreshkin et al., 2020).

283 The N-BEATS model has two primary configurations: generic and interpretable. These configurations
 284 determine how the model structures its blocks and how it processes time series data. In the generic
 285 configuration, the model uses a stack of generic blocks that are designed to be flexible and adaptable to
 286 various patterns in the time series data. Each generic block consists of fully connected layers with ReLU
 287 activation functions. The key characteristic of the generic configuration is its flexibility. Since the blocks
 288 are not specialized for any specific pattern (like trend or seasonality), they can learn a wide range of patterns
 289 directly from the data (Oreshkin et al., 2020). In the interpretable configuration, the model architecture
 290 integrates distinct trend and seasonality components. This involves structuring the basis layers at the stack
 291 level specifically to model these elements, allowing the stack outputs to be more easily understood.

292 **Trend Model:** In this stack $g_{s,l}^b$ and $g_{s,l}^f$ are polynomials of a small degree p , functions that vary slowly
 293 across the forecast window, to replicate monotonic or slowly varying nature of trends:

$$\hat{y}_{s,l} = \sum_{i=0}^p \theta_{s,l,i}^f t^i \quad (\text{Equation 10})$$

294 The time vector $t = [0, 1, 2, \dots, H-2, H-1]^T/H$ is specified on a discrete grid ranging from 0 to
 295 $(H-1)/H$, projecting H steps into the future. Consequently, the trend forecast represented in matrix form is:

$$\hat{y}_{s,l}^{tr} = T \theta_{s,l}^f \quad (\text{Equation 11})$$

296 Where the polynomial coefficients, $\theta_{s,l}^f$, predicted by an FC network at layer l of stack s , are described by
 297 Equations (6) and (7). The matrix T , consisting of powers of t , is represented as $[1, t, \dots, t^p]$. When p is
 298 small, such as 2 or 3, it compels $\hat{y}_{s,l}^{tr}$ to emulate a trend (Oreshkin et al., 2020).

299 Seasonality model: In this stack $g_{s,l}^b$ and $g_{s,l}^f$ are periodic functions, to capture the cyclical and recurring
 300 characteristics of seasonality, such that $y_t = y_{t-\Delta}$, where Δ is the seasonality period. The Fourier series
 301 serves as a natural foundation for modeling periodic functions:

$$\hat{y}_{s,l} = \sum_{i=0}^{\frac{H}{2}-1} \theta_{s,l,i}^f \cos(2\pi i t) + \theta_{s,l,i+\lceil H/2 \rceil}^f \sin(2\pi i t) \quad (\text{Equation 12})$$

302

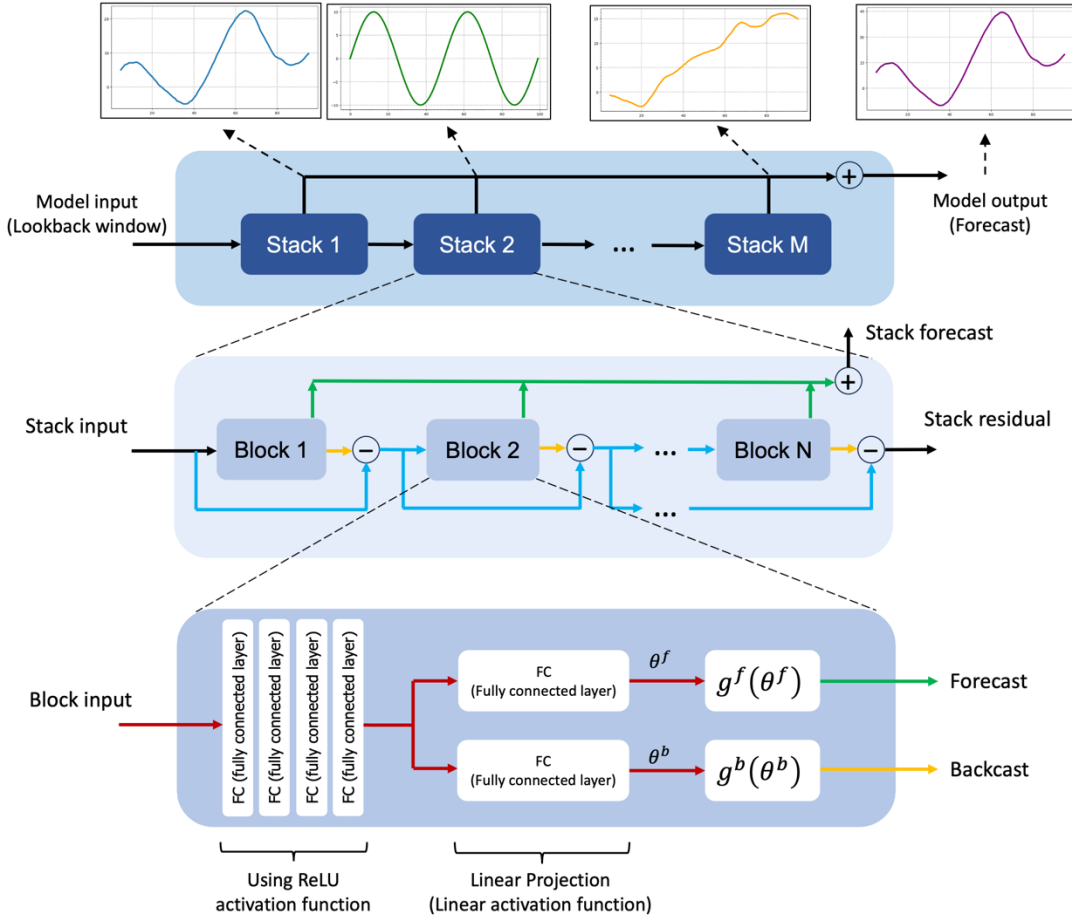
303 Consequently, the seasonality forecast is represented in the following matrix form:

$$\hat{y}_{s,l}^{seas} = S \theta_{s,l}^f \quad (\text{Equation 13})$$

$$S = [1, \cos(2\pi t), \dots, \cos\left(2\pi \left[\frac{H}{2} - 1\right] t\right), \sin(2\pi t), \dots, \sin\left(2\pi \left[\frac{H}{2} - 1\right] t\right)] \quad (\text{Equation 14})$$

304

305 Where the Fourier coefficients $\theta_{s,l}^f$, that predicted by an FC network at layer 1 of stack s , are described by
 306 Equations (6) and (7). The matrix S represents sinusoidal waveforms. As a result, the forecast $\hat{y}_{s,l}^{seas}$
 307 becomes a periodic function that imitates typical seasonal patterns (Oreshkin et al., 2020).



308

309

Figure 3. The N-BEATS modeling structure used in this research.

310 **2.2.3. N-HiTS**

311 N-HiTS builds upon the N-BEATS architecture but with improved accuracy and computational efficiency
 312 for long-horizon forecasting. N-HiTS utilizes multi-rate sampling and multi-scale synthesis of forecasts,
 313 leading to a hierarchical forecast structure that lowers computational demands and improves prediction
 314 accuracy (Challu et al., 2022).

315 Like N-BEATS, N-HiTS employs local nonlinear mappings onto foundational functions within numerous
 316 blocks. Each block includes an MLP that generates backcast and forecast output coefficients. The backcast
 317 output refines the input data for the following blocks, and the forecast outputs are combined to generate the
 318 final prediction. Blocks are organized into stacks, with each stack dedicated to grasping specific data
 319 attributes using its own distinct set of functions. The network's input is a sequence of L lags (look-back
 320 period), with S stacks, each containing B blocks (Challu et al., 2022).

321 In each block, a *MaxPool* layer with varying kernel sizes (k_l) is employed at the input, enabling the block
 322 to focus on specific input components of different scales. Larger kernel sizes emphasize the analysis of
 323 larger-scale, low-frequency data, aiding in improving long-term forecasting accuracy. This approach,
 324 known as multi-rate signal sampling, alters the effective input signal sampling rate for each block's MLP
 325 (Challu et al., 2022).

326 Additionally, multi-rate processing has several advantages. It reduces memory usage, computational
 327 demands, the number of learnable parameters, and helps prevent overfitting, while preserving the original
 328 receptive field. The following operation is applicable to the input $y_{t-L:t,l}$ of each block, with the first block
 329 ($l = 1$) using the network-wide input, where $y_{t-L:t,1} \equiv y_{t-L:t}$.

$$y_{t-L:t,l} = \text{MaxPool} (y_{t-L:t,l}, k_l) \quad (\text{Equation 15})$$

330 In many multi-horizon forecasting models, the number of neural network predictions matches the horizon's
 331 dimensionality, denoted as H . For instance, in N-BEATS, the number of predictions $|\theta_l^f| = H$. This results
 332 in a significant increase in computational demands and an unnecessary surge in model complexity as the
 333 horizon H becomes larger (Challu et al., 2022).

334 To address these challenges, N-HiTS proposes the use of temporal interpolation. This model manages the
 335 parameter counts per unit of output time ($|\theta_l^f| = [r_l H]$) by defining the dimensionality of the interpolation
 336 coefficients with respect to the expressiveness ratio r_l . To revert to the original sampling rate and predict
 337 all horizon points, this model employs temporal interpolation through the function g :

$$\hat{y}_{\tau,l} = g(\tau, \theta_l^f), \quad \forall \tau \in \{t + 1, \dots, t + H\}, \quad (\text{Equation 16})$$

$$\tilde{y}_{\tau,l} = g(\tau, \theta_l^b), \quad \forall \tau \in \{t - L, \dots, t\}, \quad (\text{Equation 17})$$

$$g(\tau, \theta) = \theta[t_1] + \left(\frac{\theta[t_2] - \theta[t_1]}{t_2 - t_1} \right) (\tau - t_1) \quad (\text{Equation 18})$$

$$t_1 = \arg \min_{t \in \tau: t \leq \tau} \tau - t, \quad t_2 = t_1 + 1/r_l \quad (\text{Equation 19})$$

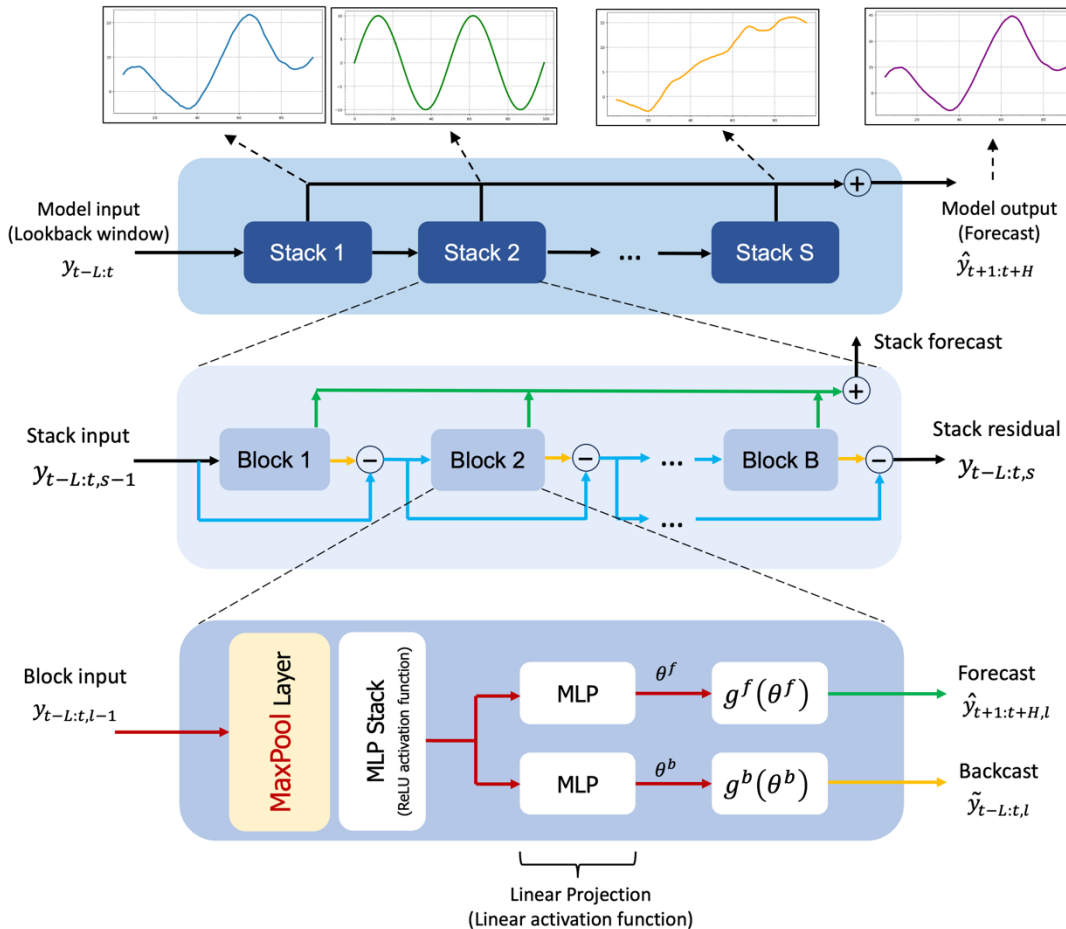
338 The hierarchical interpolation approach involves distributing expressiveness ratios over blocks, integrated
 339 with multi-rate sampling. Blocks closer to the input employ more aggressive interpolation, generating lower
 340 granularity signals. These blocks specialize in analyzing more aggressively subsampled signals. The final
 341 hierarchical prediction, $\hat{y}_{t+1:t+H}$, is constructed by combining outputs from all blocks, creating

342 interpolations at various time-scale hierarchy levels. This approach maintains a structured hierarchy of
 343 interpolation granularity, with each block focusing on its own input and output scales (Challu et al., 2022).

344 To manage a diverse set of frequency bands while maintaining control over the number of parameters,
 345 exponentially increasing expressiveness ratios are recommended. As an alternative, each stack can be
 346 dedicated to modeling various recognizable cycles within the time series (e.g., weekly, or daily) employing
 347 matching r_l . Ultimately, the residual obtained from backcasting in the preceding hierarchy level is
 348 subtracted from the input of the subsequent level, intensifying the next-level block's attention on signals
 349 outside the previously addressed band (Challu et al., 2022).

$$\hat{y}_{t+1:t+H} = \sum_{l=1}^L \hat{y}_{t+1:t+H,l} \quad (\text{Equation 20})$$

$$y_{t-L:t,l+1} = y_{t-L:t,l} - \tilde{y}_{t-L:t,l} \quad (\text{Equation 21})$$



350

351 Figure 4. The structure of N-HiTS model programmed in this study. The architecture includes several
352 Stacks, each Stack includes several Block, where each block consists of a MaxPool layer and a multi-
353 layer which learn to produce coefficients for the backcast and forecast outputs of its basis.

354 **2.3. Performance Metrics**

355 To comprehensively evaluate the accuracy of flood predictions, we utilized a suite of metrics, including
356 Nash-Sutcliffe Efficiency (NSE; Nash and Sutcliffe, 1970), persistent Nash-Sutcliffe Efficiency (persistent-
357 NSE), Kling–Gupta efficiency (KGE; Gupta et al. 2009), Root Mean Square Error (RMSE), Mean
358 Absolute Error (MAE), Peak Flow Error (PFE), and Time to Peak Error (TPE; Evin et al., 2023; Lobjigeois
359 et al., 2014). These metrics collectively facilitate a rigorous assessment of the model's performance in
360 reproducing the magnitude of observed peak flows and the shape of the hydrograph.

361 NSE measures the model's ability to explain the variance in observed data and assesses the goodness-of-fit
362 by comparing the observed and simulated hydrographs. In hydrological studies, the NSE index is a widely
363 accepted measure for evaluating the fitting quality of models (McCuen et al., 2006). It is calculated as:

$$NSE = 1 - \frac{\sum_{i=1}^n (Q_{s_i} - Q_{o_i})^2}{\sum_{i=1}^n (Q_{o_i} - \bar{Q}_o)^2} \quad (\text{Equation 22})$$

364 Where Q_{o_i} represents observed value at time i , Q_{s_i} represents simulated value at time i , \bar{Q}_o is the mean
365 observed values and n is the number of data points. An NSE value of 1 indicates a perfect match between
366 the observed and modeled data, while lower values represent the degree of departure from a perfect fit.

367 As the models are designed to predict one hour ahead, the persistent-NSE is essential for evaluating their
368 performance. The standard NSE measures the model's sum of squared errors relative to the sum of squared
369 errors when the mean observation is used as the forecast value. In contrast, persistent-NSE uses the most
370 recent observed data as the forecast value for comparison (Nevo et al., 2022). The persistent-NSE is
371 calculated as:

$$persistent - NSE = 1 - \frac{\sum_{i=1}^n (Q_{s_i} - Q_{o_i})^2}{\sum_{i=1}^n (Q_{o_i} - Q_{o_{i-1}})^2} \quad (\text{Equation 23})$$

372 Where Q_{o_i} represents the observed value at time i , Q_{s_i} represents the simulated value at time i , $Q_{o_{i-1}}$ is the
373 observed value at the last time step ($i - 1$) and n is the number of data points.

374 The KGE is a widely used performance metric in hydrological modeling and combines multiple aspects of
 375 model performance, including correlation, variability bias, and mean bias. The KGE metric is calculated
 376 using the following equation:

$$KGE = 1 - \sqrt{(r - 1)^2 + (\alpha - 1)^2 + (\beta - 1)^2} \quad (\text{Equation 24})$$

377 Where r represents Pearson correlation coefficient between observed Q_o and simulated Q_s values.
 378 α represents bias ratio, calculated as $\alpha = \frac{\mu_s}{\mu_o}$ where μ_s and μ_o are the means of simulated and observed data,
 379 respectively. β represents variability ratio, calculated as $\beta = \frac{\sigma_s/\mu_s}{\sigma_o/\mu_o}$ where σ_s and σ_o are the standard
 380 deviations of simulated and observed data, respectively.

381 RMSE quantifies the average magnitude of errors between observed and modeled values, offering insights
 382 into the absolute goodness-of-fit, while MAE is a measure of the average absolute difference between the
 383 modeled values and the observed values and provides a measure of the average magnitude of errors. RMSE
 384 is calculated as:

$$RMSE = \sqrt{\frac{1}{n} \sum_{i=1}^n (Q_{o_i} - Q_{s_i})^2} \quad (\text{Equation 25})$$

385 and MAE is calculated as:

$$MAE = \frac{1}{n} \sum_{i=1}^n |Q_{o_i} - Q_{s_i}| \quad (\text{Equation 26})$$

386 Where Q_{o_i} represents observed value at time i , Q_{s_i} represents simulated value at time i , and n is the number
 387 of data points. RMSE and MAE provide information about the magnitude of modeling errors, with smaller
 388 values indicating a better model fit.

389 PFE quantifies the magnitude disparity between observed and modeled peak flow values. The PFE metric
 390 is defined as:

$$PFE = \frac{|Q_{o_{max}} - Q_{s_{max}}|}{Q_{o_{max}}} \quad (\text{Equation 27})$$

391 Where $Q_{o_{max}}$ represents the observed peak flow value, and $Q_{s_{max}}$ signifies the simulated peak flow value.
392 The PFE metric, expressed as a dimensionless value, provides a quantitative measure of the relative error
393 in predicting peak flow magnitudes concerning the observed values. A smaller PFE denotes more accurate
394 modeling of peak flow magnitudes, with a value of zero indicating a perfect match.

395 TPE assesses the temporal alignment of peak flows in the observed and modeled hydrographs. The TPE
396 metric is computed as:

$$TPE = |T_{o_{max}} - T_{s_{max}}| \quad (\text{Equation 28})$$

397 Where $T_{o_{max}}$ signifies the time at which the peak flow occurs in the observed hydrograph, and $T_{s_{max}}$
398 represents the time at which the peak flow occurs in the simulated hydrograph. TPE that is measured in
399 units of time (hours), provides insight into the precision of peak flow timing. Smaller TPE values indicate
400 a superior alignment between the observed and modeled peak flow timing, while larger TPE values indicate
401 discrepancies in the temporal occurrence of peak flows.

402 The utilization of these five metrics, PFE, persistent-NSE, TPE, NSE, and RMSE, collectively provides a
403 robust and multifaceted assessment of flood prediction performance. This approach ensures that both the
404 magnitude and timing of peak flows, as well as the overall hydrograph shape, are accurately calibrated and
405 validated.

406 **2.4. Sensitivity and Uncertainty Analysis**

407 When implementing NN models, it's crucial to understand how each parameter affects the model's
408 performance or outputs. To achieve this, we systematically excluded each parameter from the model one
409 by one (the Leave-One-Out method). For each exclusion, we retrained the model without that specific
410 parameter and then tested its performance against a test dataset. This method helps in understanding which
411 parameters are most critical to the model's performance and which ones have a lesser impact. It also allows
412 us to identify any parameters that may be redundant or have little effect on the overall outcome, thus
413 potentially simplifying the model without sacrificing accuracy.

414 In this study, we utilized probabilistic approaches to quantify the uncertainty in flood prediction. This
415 method is rooted in statistical techniques employed for the estimation of unknown probability distributions,
416 with a foundation in observed data. More specifically, we leveraged the Maximum Likelihood Estimation
417 (MLE) approach, which entails the determination of parameter values that optimize the likelihood function.

418 The likelihood function quantifies the probability of parameters taking particular values, given the observed
 419 realizations.

420 We incorporated the MQL as a probabilistic error metric into the algorithmic architecture. MQL performs
 421 an evaluation by computing the average loss for a predefined set of quantiles. This computation is grounded
 422 in the absolute disparities between predicted quantiles and their corresponding observed values. By
 423 considering multiple quantile levels, MQL provides a comprehensive assessment of the model's ability to
 424 capture the distribution of the target variable, rather than focusing solely on point estimates.

425 The MQL metric also aligns closely with the Continuous Ranked Probability Score (CRPS), a standard tool
 426 for evaluating predictive distributions. CRPS measures the difference between the predicted cumulative
 427 distribution function and the observed values by integrating over all possible quantiles. The computation of
 428 CRPS involves a numerical integration technique that discretizes quantiles and applies a left Riemann
 429 approximation for CRPS integral computation. This process culminates in the averaging of these
 430 computations over uniformly spaced quantiles, providing a robust evaluation of the predictive distribution
 431 \hat{F}_t .

432 To calculate the 95th PPU, we utilized the 0.95 quantile level within the MQL. This quantile level directly
 433 corresponds to the 95th percentile of the predicted distribution, providing an estimate of the 95% confidence
 434 interval. By examining the model's performance at this specific quantile, we effectively assessed its ability
 435 to accurately capture the predicted values with 95% confidence.

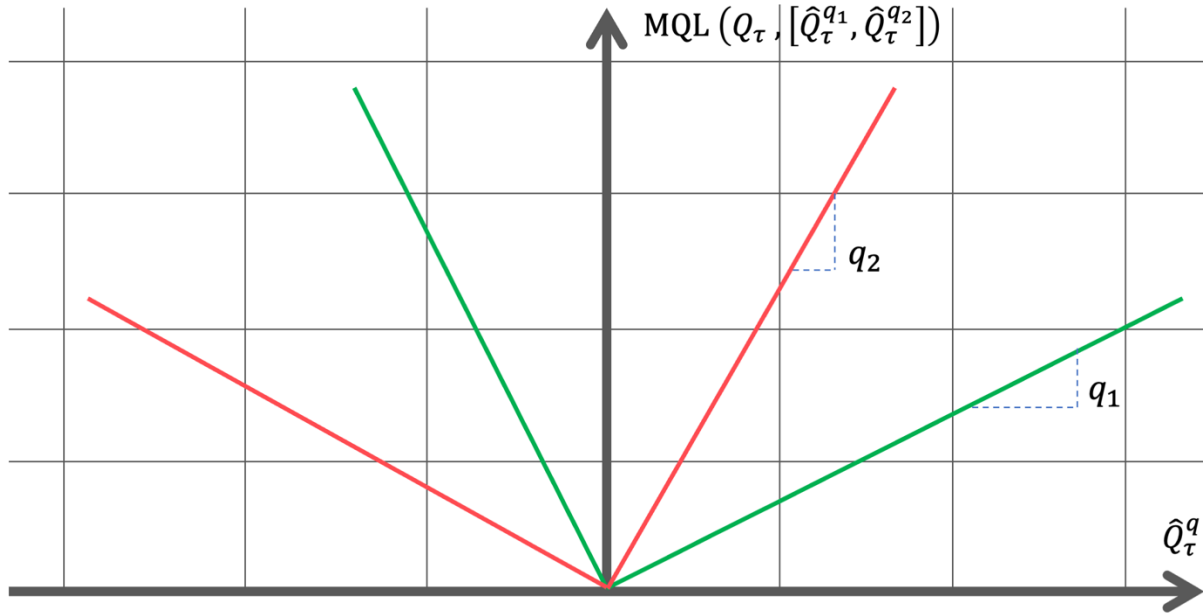
436 Incorporating MQL as a central metric in our study underscores its suitability for probabilistic forecasting,
 437 particularly in the context of uncertainty quantification. Unlike traditional error metrics that focus on point
 438 predictions, MQL captures both central tendencies and variability by penalizing errors symmetrically across
 439 quantiles. This property ensures balanced and reliable assessments of the predictive distribution, ultimately
 440 enhancing the robustness and interpretability of flood prediction models.

$$\text{MQL} (Q_\tau, [\hat{Q}_\tau^{q_1}, \dots, \hat{Q}_\tau^{q_i}]) = \frac{1}{n} \sum_{q_i} \text{QL} (Q_\tau, \hat{Q}_\tau^{q_i}) \quad (\text{Equation 29})$$

$$\text{CRPS} (Q_\tau, \hat{F}_\tau) = \int_0^1 \text{QL} (Q_\tau, \hat{Q}_\tau^{q_i}) dq \quad (\text{Equation 30})$$

$$\text{QL} (Q_\tau, \hat{Q}_\tau^q) = \frac{1}{H} \sum_{\tau=t+1}^{t+H} ((1-q)(\hat{Q}_\tau^q - Q_\tau) + q(Q_\tau - \hat{Q}_\tau^q)) \quad (\text{Equation 31})$$

441 Where Q_τ represents observed value at time τ , \hat{Q}_τ^q represents simulated value at time τ , q is the slope of the
 442 quantile loss, and H is the horizon of forecasting.



443
 444 Figure 5. The MQL function which shows loss values for different parameters of q when the true value is
 445 Q_τ .

446 Furthermore, we employed two key indices, the R-Factor and the P-Ffactor, to rigorously assess the quality
 447 of uncertainty performance in our hydrological modeling. These metrics are instrumental in quantifying the
 448 extent to which the model's predictions encompass the observed data, thereby providing valuable insights
 449 into the model's predictive accuracy and reliability.

450 The P-Factor, or percentage of data within a 95PPU, is the first index used in this assessment. The P-Factor
 451 quantifies the percentage of observed data that falls within the 95PPU, providing a measure of the model's
 452 predictive accuracy. The P-Factor can theoretically vary from 0% to a maximum of 100%. A P-Factor of
 453 100% signifies a perfect alignment between the model's predictions and the observed data within the
 454 uncertainty band. In contrast, a lower P-Factor indicates a reduced ability of the model to predict data within
 455 the specified uncertainty range.

$$P - Factor = \frac{Observations bracketed by 95PPU}{Number of observations} \times 100 \quad (\text{Equation 32})$$

456 The R-Factor can be computed by dividing the average width of the uncertainty band by the standard
 457 deviation of the measured variable. The R-Factor, with a minimum possible value of zero, provides a
 458 measure of the spread of the uncertainty relative to the variability of the observed data. Theoretically, the

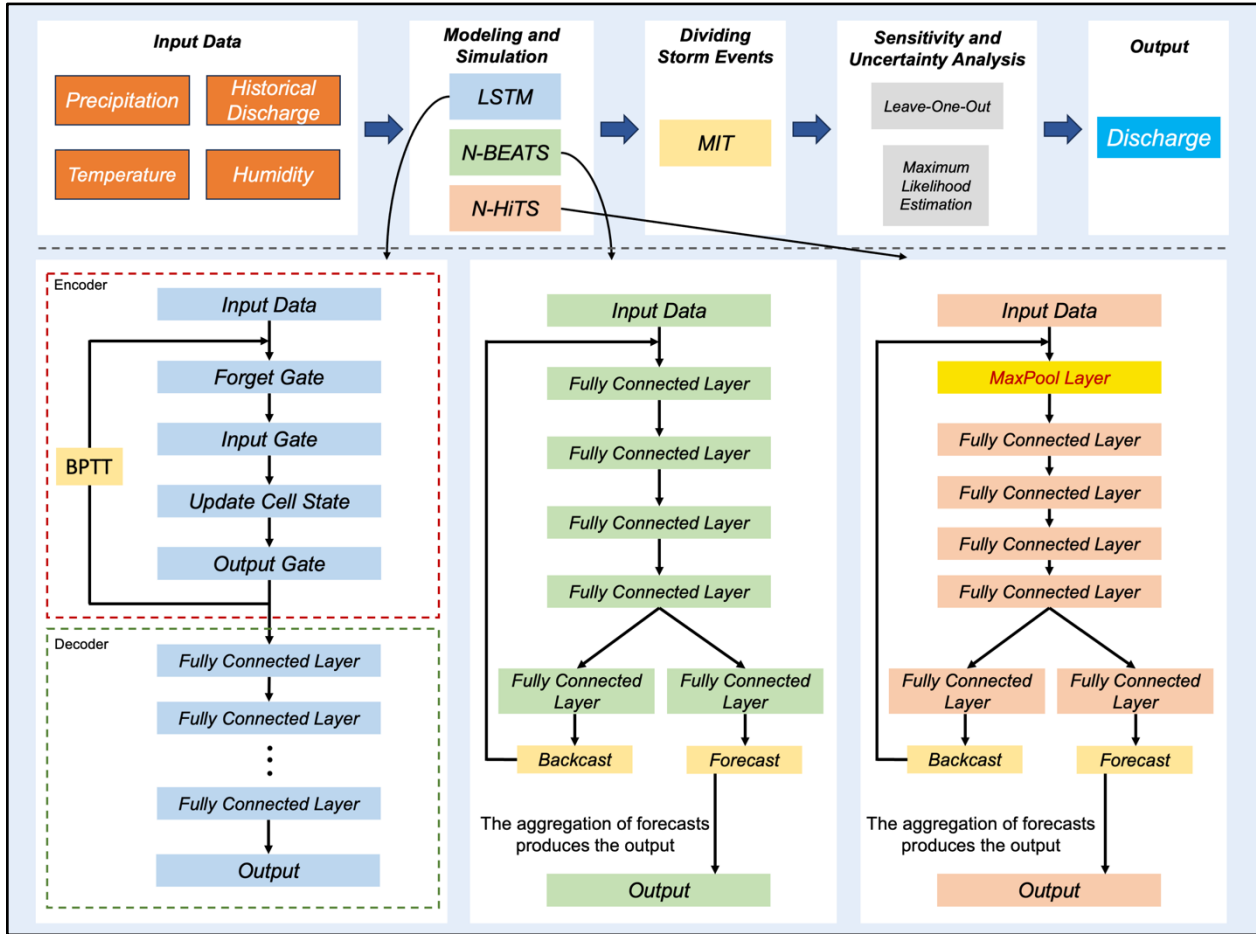
459 R-Factor spans from 0 to infinity, and a value of zero implies that the model's predictions precisely match
460 the measured data, with the uncertainty band being very narrow in relation to the variability of the observed
461 data.

$$R - Factor = \frac{\text{Average width of 95PPU band}}{\text{Standard deviation of measured variables}} \times 100 \quad (\text{Equation 33})$$

462 In practice, the quality of the model is assessed by considering the 95% prediction band with the highest P-
463 Factor and the lowest R-Factor. This specific band encompasses the majority of observed records,
464 signifying the model's ability to provide accurate and reliable predictions while effectively quantifying
465 uncertainty. A simulation with a P-Factor of 1 and an R-Factor of 0 signifies an ideal scenario where the
466 model precisely matches the measured data within the uncertainty band (Abbaspour et al., 2007).

467 Figure 6 shows the workflow of programming N-BEATS, N-HiTS, and LSTM for flood prediction. As
468 illustrated, the initial step involved cleaning and preparing the input data, which was then used to feed the
469 models. The workflow for each model and their output generation processes are depicted in Figure 6. We
470 segmented the storm events using the MIT approach, as previously described. Following this, we conducted
471 a sensitivity analysis using the Leave-One-Out method and performed uncertainty analysis using the MLE
472 approach to construct the 95PPU band. This rigorous methodology ensures a robust evaluation of model
473 performance under varying conditions and highlights the models' predictive reliability and resilience. We
474 employed the "NeuralForecast" Python package to develop the N-BEATS, N-HiTS, and LSTM models.
475 This package provides a diverse array of NN models with an emphasis on usability and robustness.

476



479 Figure 6. The workflow of N-BEATS, N-HiTS, and LSTM implementation. The upper section of the
480 figure illustrates multiple steps from data preprocessing to model evaluation. The lower section provides a
481 detailed view of the workflow and implementation for each model, highlighting the specific processes and
482 methodologies employed in generating the outputs. Backpropagation Through Time (BPTT) trains LSTM
483 by unrolling the model through time, computing gradients for each time step, and updating weights based
484 on temporal dependencies.

485 3. Results and Discussion

486 3.1. Independent Storms Delineation

487 MIT's contextual delineation of storm events laid the groundwork for in-depth evaluation of rainfall events,
488 enabling isolation and separation of rainfall events that led to significant flooding events. The nuanced
489 outcomes of the MIT assessment contributed significantly to the understanding of rainfall variability and
490 distribution as the dominant contributor to flood generation.

491 During modeling implementation, the initial imperative was the precise distinction of storm events within
492 the precipitation time series data of each case study. Our findings demonstrate that on average a dry period
493 of 7 hours serves as the optimal MIT time for both of our case studies. This outcome signifies that when a
494 dry interval of more than 7 hours transpires between two successive rainfall events, these subsequent
495 rainfalls should be considered two distinct storm events. This determination underlines the temporal
496 threshold necessary for distinguishing between individual meteorological phenomena in two case studies.

497 **3.2. Hyperparameter Optimization**

498 In the context of hyperparameter optimization, we systematically considered and tuned various
499 hyperparameters for the N-HiTS, N-BEATS, and LSTM. Following extensive exploration and fine-tuning
500 of these hyperparameters, the optimal configurations were identified (see Table 2). For the N-HiTS model,
501 the most favorable outcomes were achieved with the following hyperparameter settings: 2000 epochs,
502 "identity" for scaler type, a learning rate of 0.001, a batch size of 32, input size of 24 hours, "identity" for
503 stack type, 512 units for hidden layers of each stack, step size of 1, MQLoss as loss function, and "ReLU"
504 for the activation function. As shown in Table 2, the N-HiTS model demonstrated superior performance
505 with 4 stacks, containing 2 blocks each, and corresponding coefficients of 48, 24, 12, and 1, showcasing
506 the significance of these settings for flood prediction.

507 This hyperparameter optimization was also conducted for the N-BEATS model. In this model, we
508 considered 2000 epochs, 3 stacks with 2 blocks, "identity" for scaler type, a learning rate of 0.001, a batch
509 size of 32, input size of 24 hours, "identity" for stack type, 512 units for hidden layers of each stack, step
510 size of 1, MQLoss as loss function, and "ReLU" for the activation function.

511 Moreover, the LSTM as a benchmark model yielded its best results with 5000 epochs, an input size of 24
512 hours, "identity" as the scaler type, a learning rate of 0.001, a batch size of 32, and "tanh" as the activation
513 function. Furthermore, the LSTM's hidden state was most effective with two layers containing 128 units,
514 and the MLP decoder thrived with two layers encompassing 128 units. These meticulously optimized
515 hyperparameter settings represent the culmination of efforts to ensure that each model operates at its peak
516 potential, facilitating accurate flood prediction.

517 Table 2. Optimized values for the hyperparameters.

Hyperparameter	N-HiTS	N-BEATS	LSTM
Epoch	2000	2000	5000
Scaler type	identity	identity	standard

Learning rate	0.001	0.001	0.001
Batch size	32	32	32
Input size	24 hours	24 hours	24 hours
Stack type	Seasonality, trend, identity, identity	Seasonality, trend, identity	*
Number of units in each hidden layer	512	512	128
Loss function	MQLoss	MQLoss	MQLoss
Activation function	ReLU	ReLU	tanh
Number of stacks	4	3	*
Number of blocks in each stack	2	2	*
Stacks' coefficients	48,24,12,1	*	*

518

*Not applicable

519 In Table 2, "epoch" refers to the number of training steps, and "scaler type" indicates the type of scaler used
 520 for normalizing temporal inputs. The "learning rate" specifies the step size at each iteration while optimizing
 521 the model, and the "batch size" represents the number of samples processed in one forward and backward
 522 pass. The "loss function" quantifies the difference between the predicted outputs and the actual target
 523 values, while the "activation function" determines whether a neuron should be activated. The "stacks'
 524 coefficients" in the N-HITS model control the frequency specialization for each stack, enabling effective
 525 handling of different frequency components in the time series data.

526 Another hyperparameter for all three models is input size, which is a parameter that determines the
 527 maximum sequence length for truncated backpropagation during training and the number of autoregressive
 528 inputs (lags) that the models considered for prediction. Essentially, input size represents the length of the
 529 historical series data used as input to the model. This parameter offers flexibility in the models, allowing
 530 them to learn from a defined window of past observations, which can range from the entire historical dataset
 531 to a subset, tailored to the specific requirements of the prediction task. In the context of flood prediction,
 532 determining the appropriate input size is crucial to adequately capture the meteorological data preceding
 533 the flood event. To address this, we calculated the time of concentration (TC) of the watershed system and
 534 set the input size to exceed this duration. According to the Natural Resources Conservation Service (NRCS),
 535 for typical natural watershed conditions, the TC can be calculated from lag time, the time between peak
 536 rainfall and peak discharge, using the formula: $Lag\ time = TC \times 0.6$ (NRCS, 2009). Specifically, the

537 average TC in the Lower Dog River watershed and Upper Dutchmans Creek watershed was found to be 19
538 and 22 hours, respectively. As these represent the average TC for our case studies, we selected the 24 hours
539 for input data, slightly longer than the calculated average TC , ensuring sufficient coverage of relevant
540 meteorological data preceding all flood events.

541 **3.3. Flood Prediction and Performance Assessment**

542 In this study, we conducted a comprehensive performance evaluation of N-HiTS, N-BEATS, and
543 benchmarked these models with LSTM, utilizing two case studies: the Lower Dog River and the Upper
544 Dutchmans Creek watersheds. Within these case studies, we trained and validated the models separately
545 for each watershed across a diverse set of storm events from 01/10/2007 to 01/10/2022 (15 years) in the
546 Lower Dog River and from 21/12/1994 to 01/10/2022 (27 years) in the Upper Dutchmans Creek. The
547 decision to train separate models for each catchment was made to account for the unique hydrological
548 characteristics and local features specific to each watershed. By training models individually, we aimed to
549 optimize performance by tailoring each model to the distinct rainfall-runoff relationship inherent in each
550 catchment. All algorithms were tested using unseen flooding events that occurred between 14/12/2022 and
551 28/03/2023. In the Dog River gauging station, two winter storms i.e., January 3rd to January 5th, 2023
552 (Event 1) and February 17th to February 18th, 2023 (Event 2), as well as a spring flood event that occurred
553 during March 26th to March 28th, 2023 (Event 3) were selected for testing. Additionally, three winter
554 flooding events, i.e., December 14th to December 16th, 2022 (Event 4), January 25th and January 26th,
555 2023 (Event 5), and February 11th to February 13th, 2023 (Event 6), were chosen to test the algorithms
556 across the Killian Creek gauging station in the Upper Dutchmans Creek. The rainfall events corresponding
557 to these flooding events were delineated using the MIT technique discussed in Section 3.1.

558 Our results for the Lower Dog River case study, explicitly demonstrated the accuracy of both N-HiTS and
559 N-BEATS in generating the winter and spring flood hydrographs compared to the LSTM model across all
560 selected storm events. Although, N-HiTS prediction slightly outperformed N-BEATS during winter
561 prediction (January 3rd to January 5th, 2023). In this event, N-HiTS outperformed N-BEATS with a
562 difference of 11.6% in MAE and 20% in RMSE. The N-HiTS slight outperformance (see Tables 3 and 4)
563 is attributed to its unique structure that allows the model to discern and capture intricate patterns within the
564 data. Specifically, N-HiTS predicted flooding events hierarchically using blocks specialized in different
565 rainfall frequencies based on controlled signal projections, through expressiveness ratios, and interpolation
566 of each block. The coefficients are then used to synthesize backcast through
567 $\tilde{y}_t - L: t, l$ and forecast $(\tilde{y}_{t+1}: t + H, l)$ outputs of the block as a flood value. The coefficients were locally
568 determined along the horizon, allowing N-HiTS to reconstruct nonstationary signals over time.

569 While the N-HiTS emerged as the most accurate in predicting flood hydrograph among the three models,
570 its performance was somehow comparable with N-BEATS. The N-BEATS model exhibited good
571 performance in two case studies. It consistently provided competitive results, demonstrating its capacity to
572 effectively handle diverse storm events and deliver reliable predictions. N-BEATS has a generic and
573 interpretable architecture depending on the blocks it uses. Interpretable configuration sequentially projects
574 the signal into polynomials and harmonic basis to learn trend and seasonality components while generic
575 configuration substitutes the polynomial and harmonic basis for identity basis and larger network's depth.
576 In this study, we used interpretable architecture, as it regularizes its predictions through projections into
577 harmonic and trend basis that is well-suited for flood prediction tasks. Using interpretable architecture,
578 flood prediction was aggregated in a hierarchical fashion. This enabled the building of a very deep neural
579 network with interpretable flood prediction outputs.

580 It is essential to underscore that, despite its strong performance, the N-BEATS model did not surpass the
581 N-HiTS model in terms of NSE, Persistent-NSE, MAE, and RMSE for the Lower Dog River case study.
582 Although both models showed almost the same KGE values. Notably, the N-BEATS model showcased
583 superior results based on the PFE metric, signifying its exceptional capability in accurately predicting flood
584 peaks. However, both N-HiTS and N-BEATS models overestimated the flood peak rate of Event 2 for the
585 Lower Dog River watershed. This event, which occurred from February 17th to February 18th, 2023, was
586 flashy, short, and intense proceeded by a prior small rainfall event (from February 12th until February 13th)
587 that minimized the rate of infiltration. This flash flood event caused by excessive rainfall in a short period
588 of time (<8 hours) was challenging to predict for N-BEATS and N-HiTS models. In addition, predicting
589 the magnitude of changes in the recession curve of the third event seems to be a challenge for both models.
590 The specific part of the flood hydrograph after the precipitation event, where flood diminishes during a
591 rainless is dominated by the release of runoff from shallow aquifer systems or natural storages. It seems
592 both models showed a slight deficiency in capturing this portion of the hydrograph when the rainfall amount
593 decreases over time in the Dog River gauging station.

594 Conversely, in the Killian Creek gauging station, the N-BEATS model almost emerged as the top performer
595 in predicting the flood hydrograph based on NSE, Persistent-NSE, RMSE, and PFE performance metrics
596 (see Tables 3 and 4). KGE values remained almost the same for both models. In addition, both N-BEATS
597 and N-HiTS slightly overpredicted time to peak values for Event 5. This reflects the fact that when rainfall
598 value varies randomly around zero, it provides less to no information for the algorithms to learn the
599 fluctuations and patterns in time series data. Both N-HiTS and N-BEATS provided comparable results for
600 all events predicted in this study. N-HiTS builds upon N-BEATS by adding a MaxPool layer at each block.
601 Each block consists of an MLP layer that learns to produce coefficients for the backcast and forecast

602 outputs. This subsamples the time series and allows each stack to focus on either short-term or long-term
603 effects, depending on the pooling kernel size. Then, the partial predictions of each stack are combined using
604 hierarchical interpolation. This ability enhances N-HiTS capabilities to produce drastically improved,
605 interpretable, and computationally efficient long-horizon flood predictions.

606 In contrast, the performance of LSTM as a benchmark model lagged behind both N-HiTS and N-BEATS
607 models for all events across two case studies. Despite its extensive applications in various hydrology
608 domains, the LSTM model exhibited comparatively lower accuracy when tasked with predicting flood
609 responses during different storm events. Focusing on NSE, Persistent-NSE, KGE, MAE, RMSE, and PFE
610 metrics, it is noteworthy that all three models, across both case studies, consistently succeeded in capturing
611 peak flow rates at the appropriate timing. All models demonstrated commendable results with respect to
612 the TPE metric. In most scenarios, TPE revealed a value of 0, signifying that the models accurately
613 pinpointed the peak flow rate precisely at the expected time. In some instances, TPE reached a value of 1,
614 showing a deviation of one hour in predicting the peak flow time. This deviation is deemed acceptable,
615 particularly considering the utilization of short, intense rainfall for our analysis.

616 Our investigation into the performance of the three distinct forecasting models yielded compelling results
617 pertaining to their ability to generate 95PPU, as quantified by the P-Factor and R-Factor. These factors
618 serve as critical indicators for assessing the reliability and precision of the uncertainty bands produced by
619 the MLE. Our findings demonstrated that the N-HiTS and N-BEATS models outperformed the LSTM
620 model in mathematically defining uncertainty bands, in terms of R-Factor metric. The R-Factor, a crucial
621 metric for evaluating the average width of the uncertainty band, consistently favored the N-HiTS and N-
622 BEATS models over their counterparts. This finding was consistent across a diverse range of storm events.
623 In addition, coupling MLE with the N-HiTS and N-BEATS models demonstrated superior performance in
624 generating 95PPU when assessed through the P-Factor metric. The P-Factor represents another vital aspect
625 of uncertainty quantification, focusing on the precision of the uncertainty bands.

626 Figures 8 and 9 present graphical depictions of the predicted flood with uncertainty assessment for each
627 model as well as Flow Duration Curve (FDC) across two gauging stations. As illustrated, the uncertainty
628 bands skillfully bracketed most of the observational data, reflecting the fact that MLE was successful in
629 reducing errors in flood prediction. FDC analysis also revealed that N-HiTS and N-BEATS models
630 skillfully predicted the flood hydrograph, however, both models were particularly successful in predicting
631 moderate to high flood events (1800-6000 and >6000 cfs). In the FDC plots, the x-axis denotes the
632 exceedance probability, expressed as a percentage, while the y-axis signifies flood in cubic feet per second.
633 Notably, these plots reveal distinctive patterns in the performance of the N-HiTS, N-BEATS, and LSTM

634 models. Within the lower exceedance probability range, particularly around the peak flow, the N-HiTS and
 635 N-BEATS models demonstrated a clear superiority over the LSTM model, closely aligning with the
 636 observed data. This observed trend is consistent when examining the corresponding hydrographs. Across
 637 all events, the flood hydrographs generated by N-HiTS and N-BEATS exhibited a closer resemblance to
 638 the observed data, particularly in the vicinity of the peak timing and rate, compared to the hydrographs
 639 produced by the LSTM model. These findings underscore the enhanced predictive accuracy and reliability
 640 of the N-HiTS and N-BEATS models, particularly in predicting moderate to high flood events as well as
 641 critical hydrograph features such as peak flow rate and timing. The alignment of model-generated FDCs
 642 and hydrographs with observed data in the proximity of peak flow further establishes the efficiency of N-
 643 HiTS and N-BEATS in accurately reproducing the dynamics of flood generation mechanisms across two
 644 headwater streams.

645

646 Table 3. The performance metrics for the Lower Dog River flood predictions.

Model	Performance Metric	Event 1	Event 2	Event 3
N-HiTS	NSE	0.995	0.991	0.992
	Persistent-NSE	0.947	0.931	0.948
	KGE	0.977	0.989	0.976
	RMSE	123.2	27.6	68.5
	MAE	64.1	12.0	37.8
	PFE	0.018	0.051	0.015
	TPE (hours)	0	1	0
	P-Factor	96.9 %	100 %	93.5 %
	R-Factor	0.27	0.40	0.33
N-BEATS	NSE	0.991	0.989	0.993
	Persistent-NSE	0.917	0.916	0.956
	KGE	0.984	0.984	0.98
	RMSE	154.1	30.5	62.5
	MAE	72.6	13.6	35.9
	PFE	0.0005	0.031	0.0002
	TPE (hours)	0	1	0
	P-Factor	87.8 %	100 %	90.3 %
	R-Factor	0.17	0.23	0.24
LSTM	NSE	0.756	0.983	0.988

Persistent-NSE	-1.44	0.871	0.929
KGE	0.765	0.978	0.971
RMSE	841.1	37.9	79.5
MAE	369.4	18.6	42
PFE	0.258	0.036	0.016
TPE (hours)	1	0	0
P-Factor	81.8 %	93.1 %	96.7 %
R-Factor	0.37	0.51	0.6

647

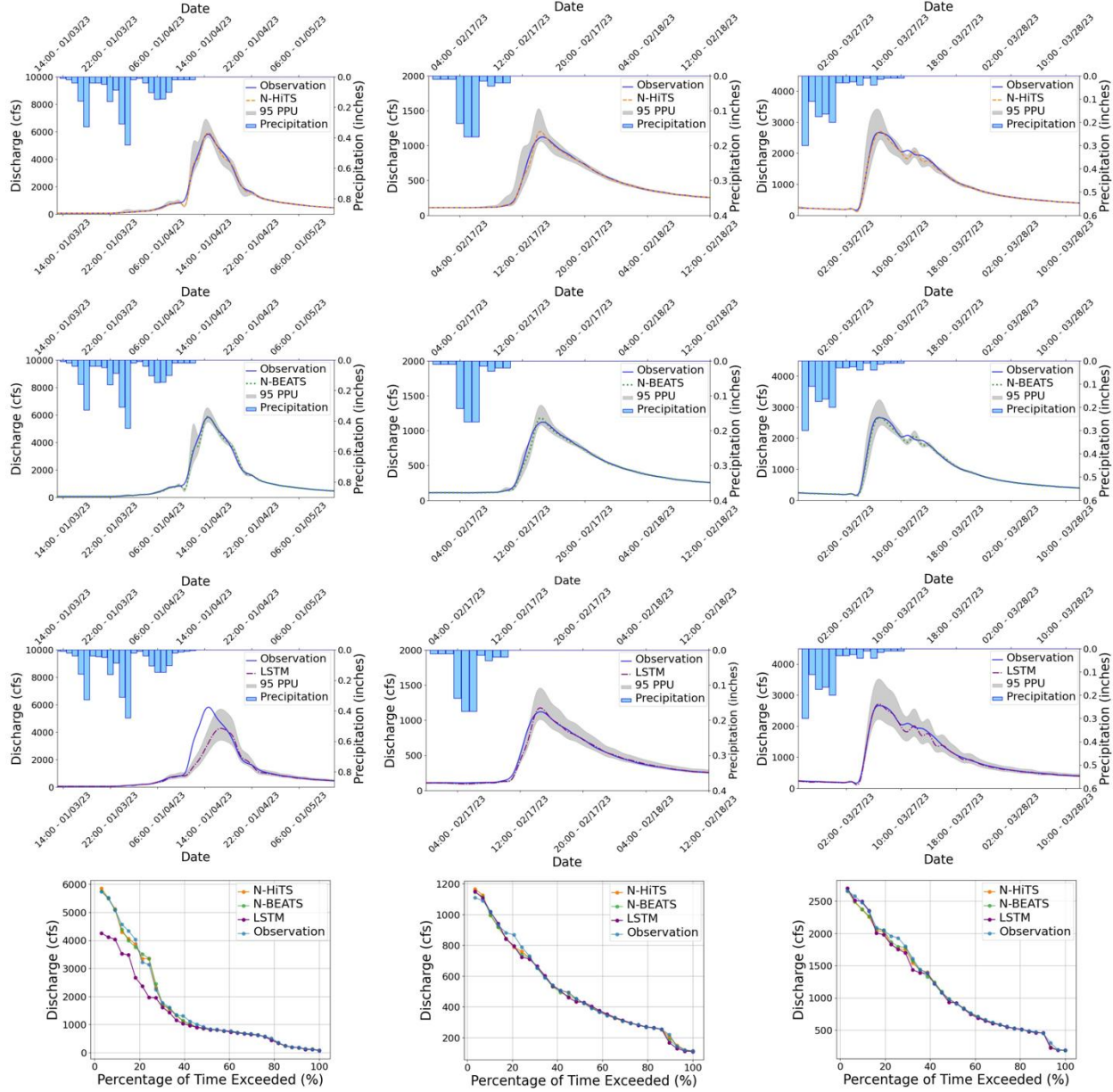
648

Table 4. The performance metrics for the Killian Creek flood predictions.

Model	Performance Metric	Event 4	Event 5	Event 6
N-HiTS	NSE	0.991	0.971	0.991
	Persistent-NSE	0.885	0.806	0.844
	KGE	0.982	0.967	0.991
	RMSE	28.8	46.0	19.0
	MAE	17.9	23.8	11.5
	PFE	0.017	0.008	0.020
	TPE (hours)	0	0	0
	P-Factor	92.6 %	90.9 %	100 %
	R-Factor	0.39	0.48	0.45
N-BEATS	NSE	0.992	0.973	0.989
	Persistent-NSE	0.908	0.821	0.823
	KGE	0.972	0.951	0.973
	RMSE	25.7	44.2	20.2
	MAE	18.3	25.9	14.0
	PFE	0.006	0.008	0.019
	TPE (hours)	0	0	0
	P-Factor	96.3 %	86.3 %	96.9 %
	R-Factor	0.43	0.53	0.43
LSTM	NSE	0.952	0.892	0.935
	Persistent-NSE	0.4	0.27	0.087
	KGE	0.92	0.899	0.901

RMSE	65.7	89.2	50.3
MAE	41.1	45	35.9
PFE	0.031	0.058	0.098
TPE (hours)	1	0	0
P-Factor	70.4 %	72.73 %	81.82 %
R-Factor	0.66	0.7	0.65

649



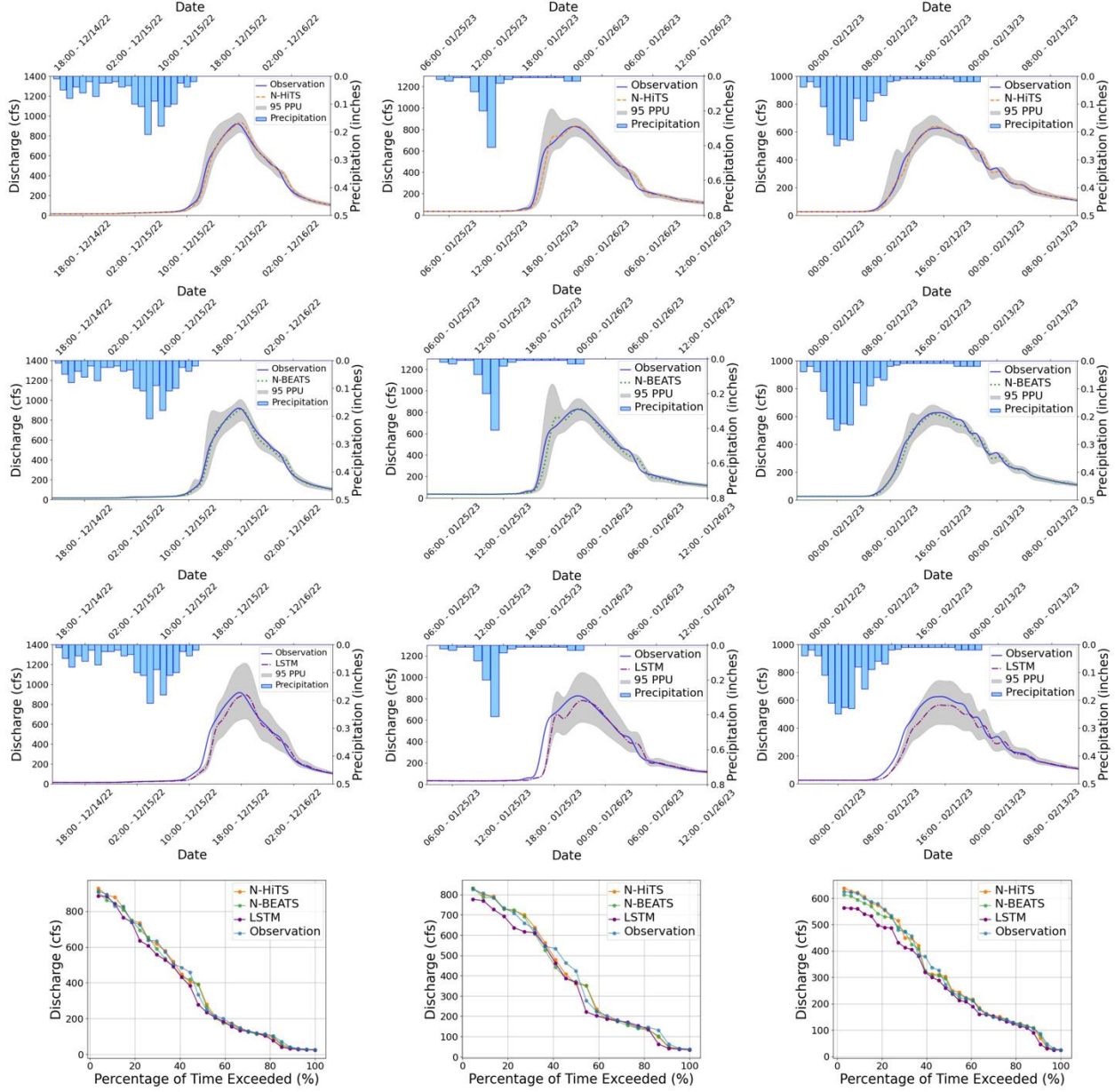
Event 1

Event 2

Event 3

650

651 Figure 7. 95 PPU band and FDC plots of N-HiTS, N-BEATS, and LSTM models for the three selected
652 flooding events in the Lower Dog River gauging station.



653
654 Figure 8. 95 PPU band and FDC plots of N-HiTS, N-BEATS, and LSTM models for the three selected
655 flooding events in the Killian Creek gauging station.

656 In our investigation, we conducted an analysis to assess the impact of varying input sizes on the performance
657 of the N-HiTS, as the best model. We implemented four different durations as input sizes to observe the
658 corresponding differences in modeling performance. Notably, one of the key metrics affected by changes
659 in input size was 95PPU, which exhibited a general decrease with increasing input size.

660 As detailed in Table 5, we observed a discernible trend in the R-Factor of the N-HiTS model as the input
661 size was increased. Specifically, there was a decline in the R-Factor as the input size expanded. This trend

662 underscores the influence of input size on model performance, particularly in terms of 95PPU band and
663 accuracy.

664 Overall, uncertainty analysis revealed that coupling MLE with N-HiTS and N-BEATS models
665 demonstrated superior performance in generating 95PPU, effectively reducing errors in flood prediction.
666 The MLE approach was more successful in reducing 95PPU bands of N-HiTS and N-BEATS models
667 compared to the LSTM, as indicated by the R-Factor and P-Factor. The N-BEATS model demonstrated a
668 narrower uncertainty band (lower R-Factor value), while the N-HiTS model provided higher precision.
669 Furthermore, incorporating data with various sizes into the N-HiTS model led to a narrower 95PPU and an
670 improvement in the R-Factor, highlighting the significance of input size in enhancing model accuracy and
671 reducing uncertainty.

Table 5. N-HiTS's R-Factor results for three storm events in each case study, using 1 hour, 2 hours, 12 hours, and 24 hours input size in training.

Input Size	1 hour	6 hours	12 hours	24 hours
Dog River, GA - Event 1	0.314	0.337	0.29	0.272
Dog River, GA - Event 2	0.35	0.413	0.403	0.402
Dog River, GA - Event 3	0.358	0.459	0.374	0.336
Killian Creek, NC - Event 4	0.491	0.422	0.426	0.388
Killian Creek, NC - Event 5	0.584	0.503	0.557	0.483
Killian Creek, NC - Event 6	0.482	0.42	0.446	0.454

672

673 **3.4. Sensitivity Analysis**

674 In this study, we conducted a comprehensive sensitivity analysis of the N-HiTS, N-BEATS, and LSTM
675 models to evaluate their responsiveness to meteorological variables, specifically precipitation, humidity,
676 and temperature. The goal was to assess how the omission of input parameters impacts the overall
677 modeling performance compared to their full-variable counterparts.

678 To execute this analysis, we systematically trained each model by excluding meteorological variables one
679 or more at a time, subsequently evaluating their predictive performance using the entire testing dataset.

680 The results of our analysis indicated that N-HiTS and N-BEATS models exhibited minimal sensitivity to
681 meteorological variables, as evidenced by the negligible impact on their performance metric (i.e., NSE,
682 Persistent-NSE, KGE, RMSE, and MAE) upon parameter exclusion.

683 Notably, as shown in Table 6, the performance of the N-HiTS model displayed a marginal deviation
684 under variable omission, while the N-BEATS model exhibited consistent performance irrespective of the

685 inclusion or exclusion of meteorological variables. The structure of this algorithm is based on backward
 686 and forward residual links for univariate time series point forecasting which does not take into account
 687 other parameters in the prediction task. These findings suggest that the predictive capabilities of N-HiTS
 688 and N-BEATS models predominantly rely on historical flood data. Both models demonstrated strong
 689 performance even without incorporating precipitation, temperature, or humidity data, underscoring their
 690 ability in flood prediction in the absence of specific meteorological inputs. This capability underscores the
 691 robustness of the N-HiTS and N-BEATS models, positioning them as viable tools and perhaps
 692 appropriate for real-time flood forecasting tasks where direct meteorological data may be limited or
 693 unavailable.

694

695 Table 6. Performance metrics' values for N-HiTS, N-BEATS, and LSTM models by excluding
 696 meteorological variables one or more at a time.

Model	Excluded Variables	NSE	Persistent- NSE	KGE	RMSE	MAE
N-HiTS	Using all variables	0.996	0.92	0.988	22.66	4.19
	Without Precipitation	0.993	0.91	0.97	23.28	4.31
	Without Humidity	0.995	0.914	0.976	22.87	4.22
	Without Temperature	0.995	0.921	0.985	22.43	4.14
	Discharge only prediction	0.993	0.911	0.972	23.21	4.29
N-BEATS	Using all variables	0.994	0.978	0.992	11.80	2.13
	Without Precipitation	0.994	0.978	0.991	11.86	2.17
	Without Humidity	0.994	0.978	0.991	11.81	2.16
	Without Temperature	0.994	0.978	0.991	11.82	2.16
	Discharge only prediction	0.994	0.978	0.991	11.96	2.17
Using all variables		0.992	0.865	0.926	29.52	8.15

	Without Precipitation	0.979	0.665	0.892	39.46	19.83
	Without Humidity	0.991	0.843	0.925	31.73	9.15
LSTM	Without Temperature	0.983	0.628	0.872	48.95	11.49
	Discharge only prediction	0.976	0.576	0.692	52.28	33.5

697

698 **3.5 Computational Efficiency**

699 The computational efficiency of the N-HiTS, N-BEATS, and LSTM models, as well as a comparative
700 analysis, is presented in Table 7. The study encompassed the entire process of training and predicting over
701 the testing period, employing the optimized hyperparameters as previously described. Regarding the
702 training time, it is noteworthy that the LSTM model exhibited the quickest performance. Specifically,
703 LSTM demonstrated a training time that was 71% faster than N-HiTS and 93% faster than N-BEATS in
704 the Lower Dog River watershed, while it was respectively, 126% and 118% faster than N-HiTS and N-
705 BEATS in the Upper Dutchmans Creek, over training dataset. This is because LSTM has a simple
706 architecture compared to the N-BEATS and N-HiTS and does not require multivariate features, hierarchical
707 interpolation, and multi-rate data sampling. Perhaps, this outcome underscores the computational advantage
708 of LSTM over other algorithms.

709 Conversely, during the testing period, the N-HiTS model emerged as the fastest and delivered the most
710 efficient results in comparison to the other models. Notably, N-HiTS displayed a predicting time that was
711 33% faster than LSTM and 32% faster than N-BEATS. This finding highlights the computational efficiency
712 of the N-HiTS model in the context of predicting processes. Our experiments unveiled an interesting
713 contrast in the computational performance of these models. While LSTM excelled in terms of training time,
714 it lagged behind when it came to the testing period.

715 In the grand scheme of computational efficiency, model accuracy, and uncertainty analysis results, it
716 becomes evident that the superiority of the N-HiTS and N-BEATS models in terms of accuracy and
717 uncertainty analysis holds paramount importance. This significance is accentuated by the critical nature of
718 flood prediction, where precision and certainty are pivotal. Therefore, computational efficiency must be
719 viewed in the context of the broader objectives, with the accuracy and reliability of flood predictions taking
720 precedence in ensuring the safety and preparedness of the affected regions.

721

722 Table 7. Computational costs of N-HiTS, N-BEATS, and LSTM models in the Dog River and Killian
 723 Creek gauging stations.

Model	Training Time over Train Datasets		Predicting Time over Test Datasets	
	(seconds)		(seconds)	
	Lower Dog River	Upper Dutchmans Creek	Lower Dog River	Upper Dutchmans Creek
N-HiTS	256.032	374.569	1533.029	1205.526
N-BEATS	288.511	361.599	2028.068	1482.305
LSTM	149.173	165.827	2046.140	1792.444

724

725 **4. Conclusion**

726 This study examined multiple NN algorithms for flood prediction. We selected two headwater streams with
 727 minimal human impacts to understand how NN approaches can capture flood magnitude and timing for
 728 these natural systems. In conclusion, our study represents a pioneering effort in exploring and advancing
 729 the application of NN algorithms, specifically the N-HiTS and N-BEATS models, in the field of flood
 730 prediction. In our case studies, both N-HiTS and N-BEATS models achieved state-of-the-art results,
 731 outperforming LSTM as a benchmark model, particularly in one-hour prediction. While a one-hour lead
 732 time may seem brief, it is highly significant for accurate flash flood prediction particularly in an area with
 733 a proximity to large metropolitan cities, where rapid response is critical. These benchmarking results are
 734 arguably a pivotal part of this research. However, the N-BEATS model slightly emerged as a powerful and
 735 interpretable tool for flood prediction in most selected events.

736 In addition, the results of the experiments described above demonstrated that N-HiTS multi-rate input
 737 sampling and hierarchical interpolation along with N-BEATS interpretable configuration are effective in
 738 learning location-specific runoff generation behaviors. Both algorithms with an MLP-based deep neural
 739 architecture with backward and forward residual links can sequentially project the data signal into
 740 polynomials and harmonic basis needed to predict intense storm behaviors with varied magnitudes. The
 741 innovation in this study – besides benchmarking the LSTM model for headwater streams – was to tackle
 742 volatility and memory complexity challenges, by locally specializing flood sequential predictions into the
 743 data signal's frequencies with interpretability, and hierarchical interpolation and pooling. Both N-HiTS and
 744 N-BEATS models offered similar performance as compared with the LSTM but also offered a level of
 745 interpretability about how the model learns to differentiate aspects of complex watershed-specific behaviors
 746 via data. The interpretability of N-HiTS and N-BEATS models stems from their designs. N-HiTS aims to
 747 enhance the accuracy of long-term time-series forecasts through hierarchical interpolation and multi-scale

748 data sampling, allowing it to focus on different data patterns, which prioritizes features essential to
749 understand flood magnitudes. N-BEATS leverages interpretable configurations with trend and seasonality
750 projections, enabling it to decompose time series data into intuitive components. N-BEATS interpretable
751 architecture is recommended for scarce data settings (such as flooding event), as it regularizes its
752 predictions through projections unto harmonic and trend basis. These approaches improve model
753 transparency by allowing understanding of how each part of the model contributes to the final prediction,
754 particularly when applied to complex flood patterns. Both models also support multivariate series (and
755 covariates) by flattening the model inputs to a 1-D series and reshaping the outputs to a tensor of appropriate
756 dimensions. This approach provides flexibility to handle arbitrary numbers of features. Furthermore, both
757 N-HiTS and N-BEATS models also support producing probabilistic predictions by specifying a likelihood
758 parameter. In terms of sensitivity analysis, both N-HiTS and N-BEATS models maintain consistent
759 performance even when trained without specific meteorological inputs. Although, during some flashy
760 floods, the models encountered challenges in capturing the peak flows and the dynamics of the recession
761 curve, which is directly related to groundwater contribution to flood hydrograph, both models were
762 technically insensitive to rainfall data as an input variable. This suggests the fact that both algorithms can
763 learn patterns in discharge data without requiring meteorological input. This ability underscores these
764 models' robustness in generating accurate predictions using historical flood data alone, making them
765 valuable tools for flood prediction, especially in data-poor watersheds or even for real-time flood prediction
766 when near real-time meteorological inputs are limited or unavailable. In terms of computational efficiency,
767 both N-HiTS and N-BEATS are trained almost at the same pace; however, N-HiTS predicted the test data
768 much quicker than N-BEATS. Unlike N-HiTS and N-BEATS, LSTM excelled in reducing training time
769 due to its simplicity and limited number of parameters.

770 Moving forward, it is worth mentioning that predicting the magnitude of the recession curve of flood
771 hydrographs was particularly challenging for all models. We argue that this is because the relation between
772 base flow and time is particularly hard to calibrate due to ground-water effluent that is controlled by
773 geological and physical conditions (vegetation, wetlands, wet meadows) in headwater streams. In addition,
774 the situations of runoff occurrence are diverse and have a high measurement variance with high frequency
775 that can make it difficult for the algorithms to fully capture discrete representation learning on time series.
776 In future studies, it will be important to develop strategies to derive analogs to the interpretable
777 configuration as well as multi-rate input sampling, hierarchical interpolation, and backcast residual
778 connections that allow for the dynamic representation of flood times series data with different frequencies
779 and nonlinearity. A dynamic representation of flood time series is, at least in principle, possible by
780 generating additive predictions in different bands of the time-series signals, reducing memory footprint and
781 compute time, and improving architecture parsimony and accuracy. This would allow the model to “learn”

782 interpretability and hierarchical representations from raw data to reduce complexity as the information
783 flows through the network. Moreover, it is noteworthy that while a single station offers valuable localized
784 data, particularly for smaller watersheds such as headwater streams where runoff is closely tied to
785 immediate meteorological conditions, it may not fully capture the spatial heterogeneity of larger
786 watersheds. For our specific case, the methods applied herein captured runoff magnitude and dynamics in
787 small watersheds using a single station. However, we recognize that for broader areas, incorporating
788 spatially distributed data would likely enhance model accuracy. Lastly, one could explore the idea of
789 enhancing N-HiTS and N-BEATS (or NN algorithms, in general) performance with uncertainty
790 quantification by using more robust Bayesian inference such as Bayesian Model Averaging (BMA) with
791 fixed and flexible prior distributions (see Samadi et al., 2020) and/or Markov Chain Monte-Carlo
792 optimization methods (Duane et al., 1987) addressing both aleatoric and epistemic uncertainties. We leave
793 these approaches for future discussion and exploration in the context of flood neural time series prediction.
794

795 **5. Acknowledgements**

796 This research is supported by the US National Science Foundation Directorate of Engineering (Grant #
797 CMMI 2125283). All opinions, findings, and conclusions or recommendations expressed in this material
798 are those of the authors and do not necessarily reflect the views of the NSF. The authors acknowledge and
799 appreciate Thorsten Wagener (University of University of Potsdam, Germany) discussion and feedback on
800 this manuscript. Clemson University (USA) is acknowledged for generous allotment of computing time on
801 the Palmetto cluster.

802 **803 6. Open Research**

804 The historical discharge data used in this study are from the USGS
805 (https://waterdata.usgs.gov/nwis/uv/?referred_module=sw), meteorological data from USDA
806 (<https://www.ncdc.noaa.gov/cdo-web/datatools/lcd>). We have uploaded the datasets and codes
807 used in this research to Zenodo, accessible via <https://zenodo.org/records/13343364>. For
808 modeling, we used the NeuralForecast package (Olivares et al., 2022), available at:
809 <https://github.com/Nixtla/neuralforecast>.

810 811 **7. References**

812 Abbaspour, K.C., Yang, J., Maximov, I., Siber, R., Bogner, K., Mieleitner, J., Zobrist, J., Srinivasan, R.,
813 2007. Modelling hydrology and water quality in the pre-alpine/alpine Thur watershed using SWAT.
814 Journal of Hydrology 333, 413–430. <https://doi.org/10.1016/j.jhydrol.2006.09.014>

815 Alaa, A.M., van der Schaar, M., 2019. Attentive State-Space Modeling of Disease Progression, in:
816 Advances in Neural Information Processing Systems. Curran Associates, Inc.

817 Asquith, W.H., Roussel, M.C., Thompson, D.B., Cleveland, T.G., Fang, X., 2005. Summary of
818 dimensionless Texas hyetographs and distribution of storm depth developed for Texas Department
819 of Transportation research project 0-4194 (No. 0-4194-4). Texas Department of Transportation.

820 Barnard, P.L., van Ormondt, M., Erikson, L.H., Eshleman, J., Hapke, C., Ruggiero, P., Adams, P.N.,
821 Foxgrover, A.C., 2014. Development of the Coastal Storm Modeling System (CoSMoS) for
822 predicting the impact of storms on high-energy, active-margin coasts. Nat Hazards 74, 1095–1125.
823 <https://doi.org/10.1007/s11069-014-1236-y>

824 Basso, S., Schirmer, M., Botter, G., 2016. A physically based analytical model of flood frequency curves.
825 Geophysical Research Letters 43, 9070–9076. <https://doi.org/10.1002/2016GL069915>

826 Challu, C., Olivares, K.G., Oreshkin, B.N., Garza, F., Mergenthaler-Canseco, M., Dubrawski, A., 2022.
827 N-HiTS: Neural Hierarchical Interpolation for Time Series Forecasting.
828 <https://doi.org/10.48550/arXiv.2201.12886>

829 Chen, Y., Li, J., Xu, H., 2016. Improving flood forecasting capability of physically based distributed
830 hydrological models by parameter optimization. Hydrology and Earth System Sciences 20, 375–
831 392. <https://doi.org/10.5194/hess-20-375-2016>

832 Clark, M.P., Nijssen, B., Lundquist, J.D., Kavetski, D., Rupp, D.E., Woods, R.A., Freer, J.E., Gutmann,
833 E.D., Wood, A.W., Brekke, L.D., Arnold, J.R., Gochis, D.J., Rasmussen, R.M., 2015. A unified
834 approach for process-based hydrologic modeling: 1. Modeling concept. Water Resources Research
835 51, 2498–2514. <https://doi.org/10.1002/2015WR017198>

836 CRED, n.d. EM-DAT - The international disaster database [WWW Document]. URL
837 <https://www.emdat.be/> (accessed 6.5.24).

838 Dasgupta, A., Arnal, L., Emerton, R., Harrigan, S., Matthews, G., Muhammad, A., O'Regan, K., Pérez-
839 Ciria, T., Valdez, E., van Osnabrugge, B., Werner, M., Buontempo, C., Cloke, H., Pappenberger,
840 F., Pechlivanidis, I.G., Prudhomme, C., Ramos, M.-H., Salamon, P., n.d. Connecting hydrological
841 modelling and forecasting from global to local scales: Perspectives from an international joint
842 virtual workshop. Journal of Flood Risk Management n/a, e12880.
843 <https://doi.org/10.1111/jfr3.12880>

844 Defontaine, T., Ricci, S., Lapeyre, C., Marchandise, A., Pape, E.L., 2023. Flood forecasting with Machine
845 Learning in a scarce data layout. IOP Conf. Ser.: Earth Environ. Sci. 1136, 012020.
846 <https://doi.org/10.1088/1755-1315/1136/1/012020>

847 Duane, S., Kennedy, A.D., Pendleton, B.J., Roweth, D., 1987. Hybrid Monte Carlo. Physics Letters B
848 195, 216–222. [https://doi.org/10.1016/0370-2693\(87\)91197-X](https://doi.org/10.1016/0370-2693(87)91197-X)

849 Erikson, L.H., Espejo, A., Barnard, P.L., Serafin, K.A., Hegermiller, C.A., O'Neill, A., Ruggiero, P.,
850 Limber, P.W., Mendez, F.J., 2018. Identification of storm events and contiguous coastal sections
851 for deterministic modeling of extreme coastal flood events in response to climate change. Coastal
852 Engineering 140, 316–330. <https://doi.org/10.1016/j.coastaleng.2018.08.003>

853 Evin, G., Le Lay, M., Fouchier, C., Mas, A., Colleoni, F., Penot, D., Garambois, P.-A., Laurantin, O.,
854 2023. Evaluation of hydrological models on small mountainous catchments: impact of the
855 meteorological forcings. <https://doi.org/10.5194/egusphere-2023-845>

856 Fan, C., Zhang, Y., Pan, Y., Li, X., Zhang, C., Yuan, R., Wu, D., Wang, W., Pei, J., Huang, H., 2019.
857 Multi-Horizon Time Series Forecasting with Temporal Attention Learning, in: Proceedings of the
858 25th ACM SIGKDD International Conference on Knowledge Discovery & Data Mining, KDD '19.
859 Association for Computing Machinery, New York, NY, USA, pp. 2527–2535.
860 <https://doi.org/10.1145/3292500.3330662>

861 Fang, K., Kifer, D., Lawson, K., Shen, C., 2020. Evaluating the Potential and Challenges of an
862 Uncertainty Quantification Method for Long Short-Term Memory Models for Soil Moisture
863 Predictions. Water Resources Research 56, e2020WR028095.
864 <https://doi.org/10.1029/2020WR028095>

865 Global assessment report on disaster risk reduction 2015 | UNDRR, 2015. URL:
866 <http://www.undrr.org/publication/global-assessment-report-disaster-risk-reduction-2015> (accessed
867 6.5.24).

868 Gotvald, A.J., 2010, Historic flooding in Georgia, 2009: U.S. Geological Survey Open-File Report 2010–
869 1230, 19 p.

870 Gupta, H.V., Kling, H., Yilmaz, K.K., Martinez, G.F., 2009. Decomposition of the mean squared error
871 and NSE performance criteria: Implications for improving hydrological modelling. Journal of
872 Hydrology 377, 80–91. <https://doi.org/10.1016/j.jhydrol.2009.08.003>

873 Hochreiter, S., Younger, A.S., Conwell, P.R., 2001. Learning to Learn Using Gradient Descent, in:
874 Dorffner, G., Bischof, H., Hornik, K. (Eds.), Artificial Neural Networks — ICANN 2001. Springer,
875 Berlin, Heidelberg, pp. 87–94. https://doi.org/10.1007/3-540-44668-0_13

876 Hsu, K., Gupta, H.V., Sorooshian, S., 1995. Artificial Neural Network Modeling of the Rainfall-Runoff
877 Process. Water Resources Research 31, 2517–2530. <https://doi.org/10.1029/95WR01955>

878 Jonkman, S.N., 2005. Global Perspectives on Loss of Human Life Caused by Floods. Nat Hazards 34,
879 151–175. <https://doi.org/10.1007/s11069-004-8891-3>

880 Kingma, D.P., Ba, J., 2017. Adam: A Method for Stochastic Optimization.
881 <https://doi.org/10.48550/arXiv.1412.6980>

882 Kratzert, F., Klotz, D., Brenner, C., Schulz, K., Herrnegger, M., 2018. Rainfall–runoff modelling using
883 Long Short-Term Memory (LSTM) networks. *Hydrology and Earth System Sciences* 22, 6005–
884 6022. <https://doi.org/10.5194/hess-22-6005-2018>

885 Lim, B., Arik, S.Ö., Loeff, N., Pfister, T., 2021. Temporal Fusion Transformers for interpretable multi-
886 horizon time series forecasting. *International Journal of Forecasting* 37, 1748–1764.
887 <https://doi.org/10.1016/j.ijforecast.2021.03.012>

888 Lobligo, F., Andréassian, V., Perrin, C., Tabary, P., Loumagne, C., 2014. When does higher spatial
889 resolution rainfall information improve streamflow simulation? An evaluation using 3620 flood
890 events. *Hydrology and Earth System Sciences* 18, 575–594. <https://doi.org/10.5194/hess-18-575-2014>

892 MacDonald, L.H., Coe, D., 2007. Influence of Headwater Streams on Downstream Reaches in Forested
893 Areas. *Forest Science* 53, 148–168. <https://doi.org/10.1093/forestscience/53.2.148>

894 Martinaitis, S.M., Wilson, K.A., Yussouf, N., Gourley, J.J., Vergara, H., Meyer, T.C., Heinselman, P.L.,
895 Gerard, A., Berry, K.L., Vergara, A. and Monroe, J., 2023. A path toward short-term probabilistic
896 flash flood prediction. *Bulletin of the American Meteorological Society*, 104(3), pp.E585-E605.

897 McCallum, B.E., and Gotvald, A.J., 2010, Historic flooding in northern Georgia, September 16–22, 2009:
898 U.S. Geological Survey Fact Sheet 2010–3061, 4 p.

899 McCuen, R.H., Knight, Z., Cutter, A.G., 2006. Evaluation of the Nash–Sutcliffe Efficiency Index. *Journal*
900 *of Hydrologic Engineering* 11, 597–602. [https://doi.org/10.1061/\(ASCE\)1084-0699\(2006\)11:6\(597\)](https://doi.org/10.1061/(ASCE)1084-0699(2006)11:6(597))

902 Munn, M., Sheibley, R., Waite, I., Meador, M., 2020. Understanding the relationship between stream
903 metabolism and biological assemblages. *Freshwater Science* 39, 680–692.
904 <https://doi.org/10.1086/711690>

905 Nash, J.E., Sutcliffe, J.V., 1970. River flow forecasting through conceptual models part I — A discussion
906 of principles. *Journal of Hydrology* 10, 282–290. [https://doi.org/10.1016/0022-1694\(70\)90255-6](https://doi.org/10.1016/0022-1694(70)90255-6)

907 Nevo, S., Morin, E., Gerzi Rosenthal, A., Metzger, A., Barshai, C., Weitzner, D., Voloshin, D., Kratzert,
908 F., Elidan, G., Dror, G., Begelman, G., Nearing, G., Shalev, G., Noga, H., Shavitt, I., Yuklea, L.,
909 Royz, M., Giladi, N., Peled Levi, N., Reich, O., Gilon, O., Maor, R., Timnat, S., Shechter, T.,
910 Anisimov, V., Gigi, Y., Levin, Y., Moshe, Z., Ben-Haim, Z., Hassidim, A., Matias, Y., 2022. Flood
911 forecasting with machine learning models in an operational framework. *Hydrology and Earth*
912 *System Sciences* 26, 4013–4032. <https://doi.org/10.5194/hess-26-4013-2022>

913 NRCS (2009). Part 630 Hydrology National Engineering Handbook, Chapter 15: Time of Concentration.

914 Olivares, K. G., Challú, C., Garza, F., Mergenthaler Canseco, M., & Dubrawski, A. (2022).
915 NeuralForecast: User friendly state-of-the-art neural forecasting models. PyCon Salt Lake City,
916 Utah, US 2022. Retrieved from <https://github.com/Nixtla/neuralforecast>

917 Olivares, K.G., Meetei, O.N., Ma, R., Reddy, R., Cao, M., Dicker, L., 2024. Probabilistic hierarchical
918 forecasting with deep Poisson mixtures. *International Journal of Forecasting* 40, 470–489.
919 <https://doi.org/10.1016/j.ijforecast.2023.04.007>

920 Oreshkin, B.N., Carpov, D., Chapados, N., Bengio, Y., 2020. N-BEATS: Neural basis expansion analysis
921 for interpretable time series forecasting. <https://doi.org/10.48550/arXiv.1905.10437>

922 Pally, R.J., Samadi, V., 2021. Application of image processing and convolutional neural networks for
923 flood image classification and semantic segmentation. *Environmental Modelling & Software* 148,
924 105285. <https://doi.org/10.1016/j.envsoft.2021.105285>

925 Palmer, T.N., 2012. Towards the probabilistic Earth-system simulator: a vision for the future of climate
926 and weather prediction. *Quarterly Journal of the Royal Meteorological Society* 138, 841–861.
927 <https://doi.org/10.1002/qj.1923>

928 Park, K., Lee, E.H., 2024. Urban flood vulnerability analysis and prediction based on the land use using
929 Deep Neural Network. *International Journal of Disaster Risk Reduction* 101, 104231.
930 <https://doi.org/10.1016/j.ijdrr.2023.104231>

931 Pourreza-Bilondi, M., Samadi, S.Z., Akhoond-Ali, A.-M., Ghahraman, B., 2017. Reliability of Semiarid
932 Flash Flood Modeling Using Bayesian Framework. *Journal of Hydrologic Engineering* 22,
933 05016039. [https://doi.org/10.1061/\(ASCE\)HE.1943-5584.0001482](https://doi.org/10.1061/(ASCE)HE.1943-5584.0001482)

934 Refsgaard, J.C., Stisen, S., Koch, J., 2022. Hydrological process knowledge in catchment modelling –
935 Lessons and perspectives from 60 years development. *Hydrological Processes* 36, e14463.
936 <https://doi.org/10.1002/hyp.14463>

937 Roelvink, D., Reniers, A., van Dongeren, A., van Thiel de Vries, J., McCall, R., Lescinski, J., 2009.
938 Modelling storm impacts on beaches, dunes and barrier islands. *Coastal Engineering* 56, 1133–
939 1152. <https://doi.org/10.1016/j.coastaleng.2009.08.006>

940 Russo, S., Perraudin, N., Stalder, S., Perez-Cruz, F., Leitao, J.P., Obozinski, G., Wegner, J.D., 2023. An
941 evaluation of deep learning models for predicting water depth evolution in urban floods.
942 <https://doi.org/10.48550/arXiv.2302.10062>

943 Safaei-Moghadam, A., Tarboton, D., Minsker, B., 2023. Estimating the likelihood of roadway pluvial
944 flood based on crowdsourced traffic data and depression-based DEM analysis. *Natural Hazards and*
945 *Earth System Sciences* 23, 1–19. <https://doi.org/10.5194/nhess-23-1-2023>

946 Saksena, S., Dey, S., Merwade, V., Singhofen, P.J., 2020. A Computationally Efficient and Physically
947 Based Approach for Urban Flood Modeling Using a Flexible Spatiotemporal Structure. *Water*
948 *Resources Research* 56, e2019WR025769. <https://doi.org/10.1029/2019WR025769>

949 Samadi, S., Pourreza-Bilondi, M., Wilson, C. a. M.E., Hitchcock, D.B., 2020. Bayesian Model Averaging
950 With Fixed and Flexible Priors: Theory, Concepts, and Calibration Experiments for Rainfall-Runoff

951 Modeling. *Journal of Advances in Modeling Earth Systems* 12, e2019MS001924.
952 <https://doi.org/10.1029/2019MS001924>

953 Scott, J., n.d. Widespread Flooding After Severe Storms - WCCB Charlotte's CW. Available at:
954 <https://www.wccbcharlotte.com/2020/02/08/widespread-flooding-after-severe-storms/> (accessed
955 6.11.24).

956 Sukovich, E.M., Ralph, F.M., Barthold, F.E., Reynolds, D.W., Novak, D.R., 2014. Extreme Quantitative
957 Precipitation Forecast Performance at the Weather Prediction Center from 2001 to 2011. *Weather*
958 and *Forecasting* 29, 894–911. <https://doi.org/10.1175/WAF-D-13-00061.1>

959 Tabas, S.S., Samadi, S., 2022. Variational Bayesian dropout with a Gaussian prior for recurrent neural
960 networks application in rainfall–runoff modeling. *Environ. Res. Lett.* 17, 065012.
961 <https://doi.org/10.1088/1748-9326/ac7247>

962 Thompson, C.M., Frazier, T.G., 2014. Deterministic and probabilistic flood modeling for contemporary
963 and future coastal and inland precipitation inundation. *Applied Geography* 50, 1–14.
964 <https://doi.org/10.1016/j.apgeog.2014.01.013>

965 Tiwari, M.K., Chatterjee, C., 2010. Development of an accurate and reliable hourly flood forecasting
966 model using wavelet-bootstrap-ANN (WBANN) hybrid approach. *Journal of Hydrology* 394, 458–
967 470. <https://doi.org/10.1016/j.jhydrol.2010.10.001>

968 Watershed Report | Office of Water | US EPA, n.d. Available at:
969 <https://watersgeo.epa.gov/watershedreport/?comid=9224629> (accessed 6.9.24).

970 Wee, G., Chang, L.-C., Chang, F.-J., Mat Amin, M.Z., 2023. A flood Impact-Based forecasting system by
971 fuzzy inference techniques. *Journal of Hydrology* 625, 130117.
972 <https://doi.org/10.1016/j.jhydrol.2023.130117>

973 Windheuser, L., Karanjit, R., Pally, R., Samadi, S., Hubig, N.C., 2023. An End-To-End Flood Stage
974 Prediction System Using Deep Neural Networks. *Earth and Space Science* 10, e2022EA002385.
975 <https://doi.org/10.1029/2022EA002385>

976 Zafarmomen, N., Alizadeh, H., Bayat, M., Ehtiat, M., Moradkhani, H., 2024. Assimilation of Sentinel-
977 Based Leaf Area Index for Modeling Surface-Ground Water Interactions in Irrigation Districts.
978 *Water Resources Research* 60, e2023WR036080. <https://doi.org/10.1029/2023WR036080>

979 Zhang, L., Qin, H., Mao, J., Cao, X., Fu, G., 2023. High temporal resolution urban flood prediction using
980 attention-based LSTM models. *Journal of Hydrology* 620, 129499.
981 <https://doi.org/10.1016/j.jhydrol.2023.129499>

982 Zhang, Y., Pan, D., Griensven, J.V., Yang, S.X., Gharabaghi, B., 2023. Intelligent flood forecasting and
983 warning: a survey. *ir* 3, 190–212. <https://doi.org/10.20517/ir.2023.12>

984 Zou, Y., Wang, J., Lei, P., Li, Y., 2023. A novel multi-step ahead forecasting model for flood based on time
985 residual LSTM. *Journal of Hydrology* 620, 129521. <https://doi.org/10.1016/j.jhydrol.2023.129521>

986